INTERNATIONAL JOURNAL FOR NUMERICAL METHODS IN ENGINEERING
Int. J. Numer. Meth. Engng 2010; **81**:604–636
Published online 29 July 2009 in Wiley InterScience (www.interscience.wiley.com). DOI: 10.1002/nme.2706

A higher-order discontinuous enrichment method for the solution of high Péclet advection–diffusion problems on unstructured meshes

C. Farhat[1,2,3,*,†], I. Kalashnikova[2] and R. Tezaur[1]

[1]*Department of Aeronautics and Astronautics, Stanford University, Stanford, CA 94305, U.S.A.*
[2]*Institute for Computational and Mathematical Engineering, Stanford University, Stanford, CA 94305, U.S.A.*
[3]*Department of Mechanical Engineering, Stanford University, Stanford, CA 94305, U.S.A.*

SUMMARY

A higher-order discontinuous enrichment method (DEM) with Lagrange multipliers is proposed for the efficient finite element solution on unstructured meshes of the advection–diffusion equation in the high Péclet number regime. Following the basic DEM methodology, the usual Galerkin polynomial approximation is enriched with free-space solutions of the governing homogeneous partial differential equation (PDE). In this case, these are exponential functions that exhibit a steep gradient in a specific flow direction. Exponential Lagrange multipliers are introduced at the element interfaces to weakly enforce the continuity of the solution. The construction of several higher-order DEM elements fitting this paradigm is discussed in detail. Numerical tests performed for several two-dimensional benchmark problems demonstrate their computational superiority over stabilized Galerkin counterparts, especially for high Péclet numbers. Copyright © 2009 John Wiley & Sons, Ltd.

Received 22 May 2009; Revised 9 June 2009; Accepted 15 June 2009

KEY WORDS: advection–diffusion; discontinuous Galerkin method; discontinuous enrichment method; high Péclet number; Lagrange multipliers; high-order

1. INTRODUCTION

The discontinuous enrichment method (DEM) was first proposed and developed in the context of the Helmholtz equation [1–3]. It was subsequently extended in [4–6] to the more general context of elastic wave propagation in fluid, solid, and fluid–solid multi-media. DEMs for

*Correspondence to: C. Farhat, Department of Aeronautics and Astronautics, 496 Lomita Mall, Stanford University, Stanford, CA 94305, U.S.A.
†E-mail: cfarhat@stanford.edu

Contract/grant sponsor: Office of Naval Research; contract/grant number: N00014-08-1-0184
Contract/grant sponsor: NDSEG Fellowship
Contract/grant sponsor: National Physical Science Consortium (NPSC) Fellowship

the finite element solution of the one-dimensional (1D) advection–diffusion equation, two-dimensional (2D) advection–diffusion equation, and the Stokes equation were also formulated in [1, 7, 8].

DEM has shown tremendous potential for solving boundary value problems (BVPs) where the solutions are characterized by rapid oscillations or large gradients. These are problems for which the standard Galerkin finite element method (FEM) does not guarantee a reasonable performance at an arbitrary mesh resolution. It is therefore inefficient and sometimes simply unfeasible. The advection–diffusion equation, often adopted as the scalar model for the linearized Navier–Stokes equations, belongs to this family of challenging problems. Indeed, in typical applications, the magnitude of the diffusion coefficient in this equation is very small compared with that of the advection coefficient—that is, the Péclet number (*Pe*), defined as the ratio of the advection and diffusion coefficients, is high. It is well-known that in this case, the solution of an advection–diffusion BVP displays sharp boundary layers. More specifically, the velocity profile rises rapidly within the thin, viscous boundary layer to the essentially constant free-stream velocity away from the wall or surface boundary. For such problems, spurious oscillations pollute the standard Galerkin FEM solutions, unless the boundary layer is resolved using a very fine mesh.

DEM can be characterized as a discontinuous Galerkin method (DGM) with Lagrange multipliers. Unlike the classical stabilized finite element methods that are often advocated for the finite element solution of advection–diffusion problems in the high Péclet regime, e.g. the streamline upwind Petrov–Galerkin (SUPG) method [9–12], adaptive stabilized finite element methods [13], Galerkin least-squares (GLS) method [14, 15], and the unusual stabilized finite element method (USFEM) [16, 17], the main idea of DEM is to enrich the standard piecewise polynomial approximations by non-conforming and *non*-polynomial basis functions that are related to the partial differential equation (PDE) to be solved. In DEM, these functions are chosen as the free-space solutions of the homogeneous constant-coefficient counterpart of the governing PDE. For many problems, they can be obtained in analytical form using standard techniques such as separation of variables. Unlike in the original partition-of-unity method (PUM) [18, 19], and other partition-of-unity-based methods such as those developed for modeling crack growth [20–22], the enrichment in DEM is performed in an additive rather than multiplicative manner. Unlike in residual free bubbles (RFB) [23–25], this enrichment is *not* constrained to vanish at the element boundaries and therefore is more effective at capturing an oscillatory or rapidly varying solution in the *entire* computational domain. Unlike in both PUM and RFB, it leads to a discontinuous rather than continuous approximation in which the enrichment degrees of freedom (dofs) can be eliminated at the element level by static condensation. This reduces computational complexity and results in a system matrix that is better conditioned than those arising from related methods such as PUM. Finally, unlike in classical discontinuous Galerkin methods (DGMs) [26–29] and other non-conforming FEMs with non-standard approximation [30, 31] in DEM, continuity of the solution across element boundaries is enforced weakly using Lagrange multipliers.

DEM has proven to be a very competitive method for acoustic scattering [2, 3], wave propagation in elastic media [5], and fluid–structure interaction [4] problems governed by the Helmholtz equation, Navier's equations, and the coupling of these equations, respectively. For example, it was shown in [3] that the discretization by three-dimensional (3D) hexahedral DEM elements of acoustic scattering problems in the medium frequency regime produces a solution of the same accuracy as that delivered by a standard high-order polynomial Galerkin approximation of comparable convergence order using four to eight times fewer dofs, and most importantly, *up to 60 times less* CPU time [3]. Similarly, impressive results were reported for DEM in [4] and [5, 6] for the

DOI: 10.1002/nme

solution of medium-frequency wave propagation problems in elastic media, and multi-scale wave propagation problems in multi-fluid and fluid–solid media, respectively.

In [7], a DEM was developed for the finite element solution of the two-dimensional (2D) advection–diffusion equation on domains discretized by uniform meshes. An enrichment basis consisting of exponential functions, each exhibiting a sharp gradient in some flow direction θ_i, was derived. Two low-order rectangular elements, denoted by $R-4-1$ and $R-5-1^+$, each with a single Lagrange multiplier dof per edge, were proposed for uniform discretizations of the computational domain. The approximation space of the enrichment-only DEM element $R-4-1$ (also referred to in this case as a DGM element) contains four exponential enrichment functions and no polynomial field. The approximation space of the genuine DEM element $R-5-1^+$ contains five exponential enrichment functions and the polynomial field of the standard Galerkin bilinear quadrilateral element Q_1. Both elements were shown in [7] to outperform standard Galerkin and stabilized Galerkin finite elements of comparable complexity and comparable order of convergence by a large margin. For non-trivial benchmark problems, they were shown to deliver numerical solutions with relative errors that were at least two, and in some cases many, orders of magnitude lower than those associated with the standard Galerkin solutions.

In this paper, the focus is kept on the 2D case, and the DEM presented in [7] is extended to higher-order elements and unstructured meshes. This extension features a general formulation of the Lagrange multiplier approximation that is applicable to any straight-edge element. Also, a special class of variant DEM elements labeled 'advection-limited' elements is presented for handling problems where $Pe>10^3$.

To this effect, the remainder of this paper is organized as follows. In Section 2, the hybrid variational formulation of DEM is reviewed in the context of the 2D advection–diffusion equation. The exponential enrichment functions constituting the approximation space $\mathscr{V}^E$ are derived in Section 3. Section 4 discusses the approximation of the Lagrange multiplier field on an arbitrarily oriented edge in a mesh with straight-edged elements. Section 5 outlines a general procedure for designing a DGM or DEM element for 2D advection–diffusion problems. Several new, higher-order quadrilateral DGM and DEM elements are described in Section 6. The computational properties of these elements are summarized in Section 7, and their performance is assessed for several benchmark problems in Section 8. Finally, conclusions are offered in Section 9.

2. FORMULATION OF DEM FOR A 2D ADVECTION–DIFFUSION BVP

Let $\Omega\subset\mathbb{R}^2$ be an open bounded domain with connected, Lipschitz continuous boundary Γ. Consider the following all-Dirichlet BVP for the advection–diffusion equation in Ω in its strong form (S)

$$(S):\begin{cases}\text{Find } u\in H^1(\Omega) \text{ such that}\\ \mathscr{L}u\equiv\mathbf{a}\cdot\nabla u-\Delta u=f \quad \text{in } \Omega\\ u=g \quad \text{on } \Gamma\end{cases} \tag{1}$$

Here, $H^1(\Omega)$ is the usual Sobolev space, $g:\Gamma\to\mathbb{R}$ is a function of Dirichlet data, $f:\Omega\to\mathbb{R}^2$ is a source term, and $\mathbf{a}^{\mathrm{T}}\equiv(a_1\ \ a_2)$ is the vector of advection-coefficients, assumed in this paper to be constant. The advection-coefficients define the advection direction whose angle with the x-axis is

DOI: 10.1002/nme

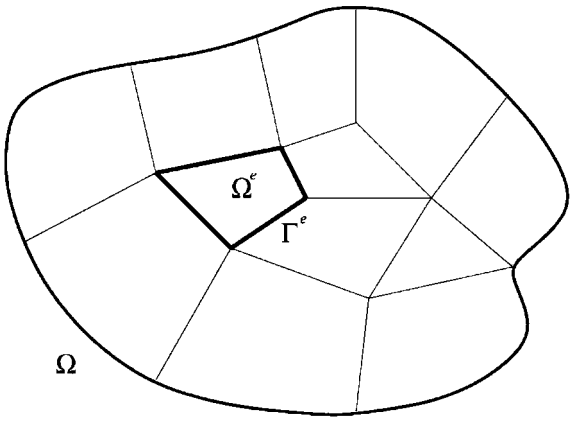

Figure 1. Decomposition of domain Ω into elements Ω^e.

denoted in this paper by ϕ and that satisfies

$$a_1 = |\mathbf{a}| \cos\phi, \quad a_2 = |\mathbf{a}| \sin\phi \tag{2}$$

Associated with the advection–diffusion equation (1) is a dimensionless parameter known as the Péclet number (Pe) defined by

$$Pe \equiv \frac{\text{rate of advection}}{\text{rate of diffusion}} = l_\Omega |\mathbf{a}| = Re \cdot \begin{cases} Pr & \text{(thermal diffusion)} \\ Sc & \text{(mass diffusion)} \end{cases} \tag{3}$$

where Re, Pr and Sc are the Reynolds, Prandtl and Schmidt numbers, respectively, and l_Ω is a characteristic length scale of the domain Ω. When Ω is a unit square or unit circle, this characteristic length is naturally chosen as $l_\Omega \equiv 1$, so that $Pe = |\mathbf{a}|$. Partition Ω into n_{el} disjoint element domains Ω^e, each with a boundary $\Gamma^e \equiv \partial\Omega^e$ (Figure 1), so that

$$\overline{\Omega} = \overline{\bigcup_{e=1}^{n_{el}} \Omega^e} \quad \text{with} \quad \bigcap_{e=1}^{n_{el}} \Omega^e = \emptyset \tag{4}$$

The unions of element interiors and element boundaries are denoted by $\tilde{\Omega}$ and $\tilde{\Gamma}$, respectively, and denoted by

$$\tilde{\Omega} = \bigcup_{e=1}^{n_{el}} \Omega^e, \quad \tilde{\Gamma} = \bigcup_{e=1}^{n_{el}} \Gamma^e \tag{5}$$

The set of element interfaces (or interior element boundaries) is denoted by

$$\Gamma_{\text{int}} = \tilde{\Gamma} \backslash \Gamma \tag{6}$$

and the intersection between two adjacent element boundaries Γ^e and $\Gamma^{e'}$ is denoted by

$$\Gamma^{e,e'} = \Gamma^e \cap \Gamma^{e'} \tag{7}$$

DOI: 10.1002/nme

2.1. Hybrid variational formulation

Let

$$\mathscr{V} \equiv \{v \in L^2(\tilde{\Omega}) : v|_{\Omega^e} \in H^1(\Omega^e)\}, \quad \mathscr{W} = \Pi_e \Pi_{e'<e} H^{-1/2}(\Gamma^{e,e'}) \times H^{-1/2}(\Gamma) \tag{8}$$

$\mathscr{V}$ is a space of element approximations of the solution and $\mathscr{W}$ is a space of Lagrange multipliers. The latter are introduced to enforce weakly the continuity of the solution across the element boundaries, as the element approximations comprising the space $\mathscr{V}$ are allowed to be discontinuous between elements.

Multiplying the first equation in (1) by a test function $v \in \mathscr{V}$ and integrating the diffusion term by parts give rise to the following weak variational form (W)

$$(W): \begin{cases} \text{Find } (u, \lambda) \in \mathscr{V} \times \mathscr{W} \text{ such that} \\ a(v,u) + b(\lambda, v) = r(v), \quad \forall v \in \mathscr{V} \\ b(\mu, u) = -r_d(\mu), \quad \forall \mu \in \mathscr{W} \end{cases} \tag{9}$$

Here, $a(\cdot,\cdot)$ and $b(\cdot,\cdot)$ are bilinear forms on $\mathscr{V} \times \mathscr{V}$ and $\mathscr{W} \times \mathscr{V}$, respectively. They are given by

$$a(v,u) \equiv (\nabla v + v\mathbf{a}, \nabla u)_{\tilde{\Omega}} = \int_{\tilde{\Omega}} (\nabla v \cdot \nabla u + v\mathbf{a} \cdot \nabla u)\, \mathrm{d}\Omega \tag{10}$$

$$b(\lambda, v) \equiv \sum_e \sum_{e'<e} \int_{\Gamma^{e,e'}} \lambda (v_{e'} - v_e)\, \mathrm{d}\Gamma + \int_{\Gamma} \lambda v\, \mathrm{d}\Gamma \tag{11}$$

and $r(v)$ and $r_d(\mu)$ are the following linear forms:

$$r(v) \equiv (f, v) = \int_{\Omega} f v\, \mathrm{d}\Omega, \quad r_d(\mu) \equiv \int_{\Gamma} \mu g\, \mathrm{d}\Gamma \tag{12}$$

In (10) and (12), $(\cdot,\cdot)$ denotes the usual L^2 inner product over Ω; in (11), $v_e \equiv v|_{\Omega^e}$. Note that the bilinear form $a(\cdot,\cdot)$ in (10) is *not* symmetric ($a(v,u) \neq a(u,v)$) for the advection–diffusion operator due to the presence of the first-order advection term.

2.2. Approximation space $\mathscr{V}^h$

Let h denote the generic size of a typical element Ω^e. Denote the finite dimensional versions of the solution approximation and Lagrange multiplier spaces defined in (8) by

$$\mathscr{V}^h \subset \mathscr{V}, \quad \mathscr{W}^h \subset \mathscr{W} \tag{13}$$

DEM [1, 7, 32] seeks an approximate solution $(u^h, \lambda^h) \in (\mathscr{V}^h, \mathscr{W}^h)$ of the variational problem (9). The discussion of the space of the Lagrange multiplier approximations $\mathscr{W}^h$ is held off until Section 4. Here, focus is set on the space of element approximations $\mathscr{V}^h$. The primal unknown $u^h \in \mathscr{V}^h$ has one of the two forms given in Table I. $\mathscr{V}^P$ is the usual space of polynomial interpolants characteristic of the classical Galerkin FEM. $\mathscr{V}^E$ is the space of so-called 'enrichment' functions u^E. It is spanned by the free-space solutions of the homogeneous form of the governing PDE that are not already represented in $\mathscr{V}^P$—that is,

$$\mathscr{V}^E \subset \{u^E \in L^2(\mathbb{R}^2) : \mathscr{L} u^E = \mathbf{a} \cdot \nabla u^E - \Delta u^E = 0\} \tag{14}$$

DOI: 10.1002/nme

Table I. Approximation spaces for DGM and DEM elements.

	$\mathscr{V}^h$	u^h
DGM	$\mathscr{V}^E$	u^E
DEM	$\mathscr{V}^P \oplus (\mathscr{V}^E \setminus \mathscr{V}^P)$	$u^P + u^E$

Since the enrichment functions are employed at an element level, they are chosen as the free-space solutions of the homogeneous *constant*-coefficient version of the governing PDE, even in the more general variable coefficient scenario $\mathbf{a} = \mathbf{a}(\mathbf{x})$ (not specifically considered in this paper). These solutions can be obtained with little difficulty using standard PDE techniques—for example, the method of separation of variables (Section 3).

Table I implies that two varieties of DEM can be defined: a genuine or 'full' DEM and an enrichment-only DEM, referred to in the remainder of this paper as in previous literature as DGM (for 'discontinuous Galerkin method') or 'pure DGM' . In the case of genuine DEM elements, the solution space $\mathscr{V}^h$ is constructed as a direct sum of $\mathscr{V}^P$ and $\mathscr{V}^E$. This splitting of the approximation into polynomials and enrichment functions can be viewed as a decomposition of the numerical solution into coarse (polynomial) and fine (enrichment) scales. It turns out that, as will be shown in Section 8, the polynomial field is not required in certain, namely homogeneous, problems. Since the enrichment field contains free-space solutions of the underlying equation to be solved, it may entirely capture the homogeneous solutions rather than merely enhance the polynomial field. This observation motivates the construction of enrichment-only DGM elements in which the contribution of the standard polynomial field is dropped from the approximation entirely, resulting in improved computational efficiency without any loss of accuracy [7, 32].

3. ENRICHMENT BASES

The basis functions defining the space $\mathscr{V}^h$ are derived by solving the homogeneous, free-space, constant coefficient advection–diffusion equation $\mathscr{L}u^E = 0$. This can be done using the standard technique of separation of variables, that is, assuming a $C^2(\Omega)$ solution of the form $u^E(x, y) = \sum_k F_k(x)G_k(y)$ and determining the functions $F_k(x), G_k(y) : \mathbb{R} \to \mathbb{R}$ such that $\mathscr{L}u^E = 0$. This leads to

$$F_k(x) = \begin{cases} e^{a_1 x/2}\left[A\exp\left(\dfrac{\sqrt{\alpha^2}}{2}x\right) + B\exp\left(-\dfrac{\sqrt{\alpha^2}}{2}x\right)\right] & \text{if } k \leqslant \dfrac{a_1^2}{4} \\ e^{a_1 x/2}\left[A\cos\left(\dfrac{\sqrt{-\alpha^2}}{2}x\right) + B\sin\left(\dfrac{\sqrt{-\alpha^2}}{2}x\right)\right] & \text{if } k > \dfrac{a_1^2}{4} \end{cases} \tag{15}$$

DOI: 10.1002/nme

$$G_k(y) = \begin{cases} e^{a_2 y/2}\left[C\exp\left(\dfrac{\sqrt{\beta^2}}{2}y\right) + D\exp\left(-\dfrac{\sqrt{\beta^2}}{2}y\right)\right] & \text{if } k \geqslant -\dfrac{a_2^2}{4} \\ e^{a_2 y/2}\left[C\cos\left(\dfrac{\sqrt{-\beta^2}}{2}y\right) + D\sin\left(\dfrac{\sqrt{-\beta^2}}{2}y\right)\right] & \text{if } k < -\dfrac{a_2^2}{4} \end{cases} \tag{16}$$

where A, B, C, D and k are real constants and

$$\alpha^2 \equiv a_1^2 - 4k, \quad \beta^2 \equiv a_2^2 + 4k \tag{17}$$

The form of the solution depends on the value of the separation of variables constant k relative to the given advection velocities a_1 and a_2. More specifically:

(i) When $-a_2^2/4 \leqslant k \leqslant a_1/4$, both F_k and G_k are exponential functions.
(ii) When $k < -a_2^2/4$, F_k is an exponential function whereas G_k is a trigonometric function.
(iii) When $k > a_1^2/4$, F_k is a trigonometric function and G_k is an exponential function.

In the first case, u^E is a rapidly rising or decaying exponential in both the x- and y-directions, whereas in the second two cases, the enrichment is oscillatory in either the x- or y-direction.

At this point, it is helpful to remark that, unless there is a trigonometric source in (1), the solutions of this BVP do *not* exhibit an oscillatory behavior. They are known to exhibit, however, sharp *exponential* boundary layers in which the velocity profile rises or falls sharply, much like the functions in case (i). Motivated by this observation, only enrichment functions that are exponential in both x and y variables are considered in this paper—that is,

$$u^E(x, y) = e^{((a_1/2) \pm \alpha/2)x} e^{((a_2/2) \pm \beta/2)y} \tag{18}$$

Different enrichment functions of the form (18) can be generated by varying the signs in (18) and the values of the constant k in (17).

The fact that the parameter k can take *any* real value from $-\infty$ to ∞ complicates the systematic construction of enrichment basis functions. For this reason, and inspired by DEM for the Helmholtz equation [1] where the enrichment functions are plane waves propagating in directions θ_i, parameterizations in which the constant k is replaced by an angle parameter $\theta_i \in [0, 2\pi)$ is sought-after here. To this effect, it is first noted that

$$\alpha^2 + \beta^2 = a_1^2 + a_2^2 \tag{19}$$

which suggests the following parametrization

$$\alpha \equiv |\mathbf{a}| \cos\theta_i, \quad \beta \equiv |\mathbf{a}| \sin\theta_i \tag{20}$$

where $\theta_i \in [0, 2\pi)$ and $|\mathbf{a}| \equiv \sqrt{a_1^2 + a_2^2}$. Substituting this parametrization into (18) gives

$$u^E(\mathbf{x}; \theta_i) = e^{1/2(a_1 + |\mathbf{a}|\cos\theta_i)x} e^{1/2(a_2 + |\mathbf{a}|\sin\theta_i)y} \tag{21}$$

Introducing the shorthand notation

$$\mathbf{a}_\theta^{\mathrm{T}} \equiv |\mathbf{a}|(\cos\theta \;\; \sin\theta), \quad \mathbf{a}_\phi^{\mathrm{T}} \equiv |\mathbf{a}|(\cos\phi \;\; \sin\phi) \tag{22}$$

DOI: 10.1002/nme

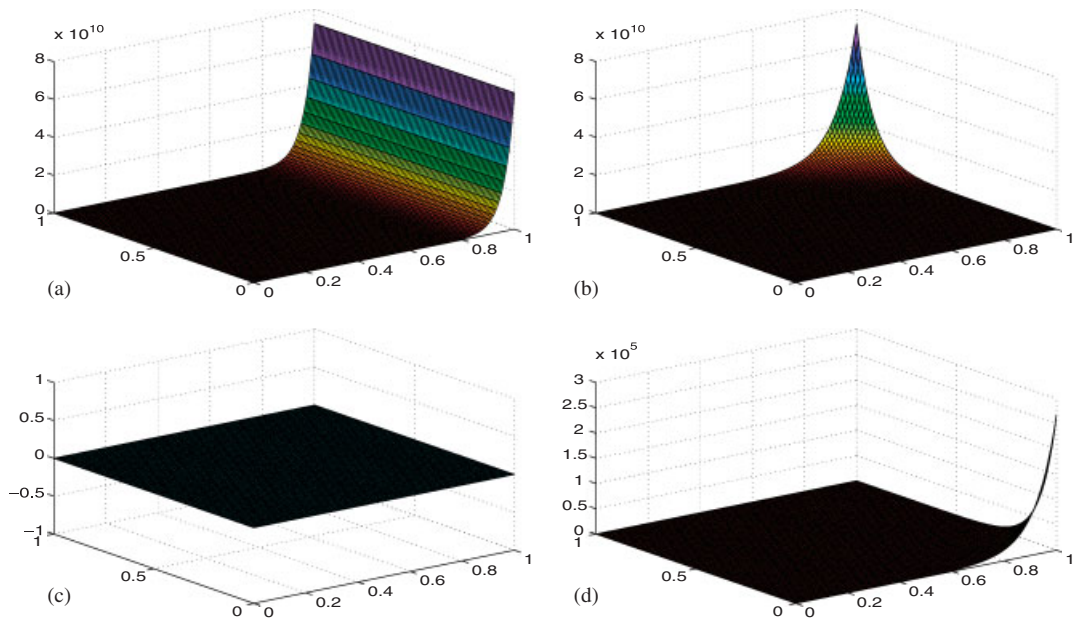

Figure 2. Plots of enrichment function $u^E(\mathbf{x};\theta_i)$ for several values of θ_i $(a_1=25, a_2=0)$. (a) $\theta_i=0$; (b) $\theta_i=\pi/2$; (c) $\theta_i=\pi$; and (d) $\theta_i=3\pi/2$.

the enrichment space $\mathscr{V}^E$ can then be written as the following superposition of the 2D exponential enrichment functions (21):

$$\mathscr{V}^E \equiv \left\{ u^E \in L^2(\tilde{\Omega}) : u|^E_{\Omega^e}(\mathbf{x}) = \sum_{i=1}^{n^E} u_i \exp\left\{ \frac{1}{2}(\mathbf{a}_{\theta_i} + \mathbf{a}_\phi)\cdot(\mathbf{x}-\mathbf{x}^e_{r,i}) \right\}, 0 \leqslant \theta_i < 2\pi, u_i \in \mathbb{R} \right\} \tag{23}$$

Here, $\mathbf{x}^e_{r,i} \in \Omega^e$ is an arbitrary reference point for the ith enrichment function $u^E(\mathbf{x};\theta_i)$, introduced within each element to alleviate the ill-conditioning of the resulting element matrices (Section 7.3). The scalar n^E denotes the number of enrichment functions (the dimension of the space $\mathscr{V}^E$), selected *a priori* to design a particular DEM element (Section 6). The set of angles $\{\theta_i\}$ specifying an enrichment basis is denoted by

$$\Theta^u \equiv \{\text{set of angles } \{\theta_i\} \text{ defining } \mathscr{V}^E\} \tag{24}$$

The natural interpretation of these angles is that they are flow directions. Not only does this interpretation fit nicely with the problem at hand, it also facilitates the design and implementation of DGM/DEM elements of arbitrary orders. To design an element with $\dim\mathscr{V}^E = n^E$, one simply selects n^E angles $\theta_i \in [0, 2\pi)$, each specifying a function of the form (21). One strategy for constructing a space $\mathscr{V}^E$ is to select the set Θ^u such that the enrichment functions implied by these angles exhibit sharp gradients in as many directions as there are basis functions. Figure 2 shows plots of the enrichment functions (21) for several angles θ_i. Of particular interest is the relationship between θ_i and the advection direction ϕ (2) implied by the advection coefficients a_1 and a_2. Setting $\theta_i = \phi$ in (21), one finds that $u^E(\mathbf{x};\phi) = e^{a_1(x-x^e_r)}e^{a_2(y-y^e_r)}$, so that $\nabla u^E(\mathbf{x};\phi) = \mathbf{a}u^E(\mathbf{x};\phi)$.

DOI: 10.1002/nme

It is a well-known fact that the gradient of a function points in the direction in which that function changes most rapidly. It follows that the enrichment function specified by $\theta_i = \phi$ changes most rapidly in the advection direction ϕ. This observation motivates including $\theta_i = \phi$ in the set Θ^u defining the enrichment basis of any DGM or DEM element.

Another convenient property of the parametrization (21) of the enrichment functions is the straight-forward inclusion of the constant basis function $u^E = \text{const}$. Indeed,

$$u^E(\mathbf{x}; \theta_i = \phi - n\pi) = 1 \tag{25}$$

for any $n \in \mathbb{Z}$. That is, a constant basis function is generated by including the angle $\theta_i = \phi - n\pi$ in the set Θ^u defining a particular DEM element (Figure 2(c)). The constant basis function should be included in the enrichment space of DGM elements, but omitted from the enrichment space of genuine DEM elements. Indeed, a constant *is* a free-space solution of the advection–diffusion equation (1) and may be present in the exact solution one hopes to capture even in the absence of a source term ($f = 0$). However, since the polynomial portion of the approximation space $\mathscr{V}^h = \mathscr{V}^E \oplus \mathscr{V}^P$ of a genuine DEM element already contains a constant, $\theta_i = \phi - n\pi$ is not be included in the set Θ^u of such an element.

4. APPROXIMATION OF THE LAGRANGE MULTIPLIERS ON UNSTRUCTURED QUADRILATERAL MESHES

Most, if not all, techniques and theoretical results established so far for approximating Lagrange multipliers have been derived in the context of standard polynomial approximations of the primal variable u^h. Extending these ideas to the case of exponential approximations u^E is not a straightforward task.

Given an approximation space $\mathscr{V}^h$, the Lagrange multiplier approximations constituting the space $\mathscr{W}^h$ can be inferred from the weak form (9) and the variational calculus. Applying the bilinear form $a(\cdot,\cdot)$ defined in (10) to $u, v, \in \mathscr{V}$ and integrating by parts the $\int_{\tilde{\Omega}} \nabla v \cdot \nabla u \, \mathrm{d}\Omega$ term gives

$$a(u,v) = \int_{\tilde{\Omega}} (\mathbf{a}\cdot\nabla u - \Delta u) v \, \mathrm{d}\Omega + \int_{\Gamma} \nabla u \cdot \mathbf{n} v \, \mathrm{d}\Gamma + \sum_e \sum_{e'} \int_{\Gamma^{e,e'}} (\nabla u^e \cdot \mathbf{n}^e v^e + \nabla u^{e'} \cdot \mathbf{n}^{e'} v^{e'}) \, \mathrm{d}\Gamma \tag{26}$$

where $\mathbf{n}^e$ (or $\mathbf{n}^{e'}$) is the outward unit normal to Γ^e (or $\Gamma^{e'}$). Substituting (26) into the first equation in the weak form (9) leads to

$$\lambda = \nabla u_e \cdot \mathbf{n}^e = -\nabla u_{e'} \cdot \mathbf{n}^{e'} \quad \text{on } \Gamma^{e,e'} \tag{27}$$

and

$$\lambda = -\nabla u \cdot \mathbf{n} \quad \text{on } \Gamma \tag{28}$$

if a Dirichlet boundary condition is to be enforced on Γ. The result (27) suggests choosing

$$\lambda^h \approx \nabla u_e^E \cdot \mathbf{n}^e = -\nabla u_{e'}^E \cdot \mathbf{n}^{e'} \quad \text{on } \Gamma^{e,e'} \tag{29}$$

as a good approximation of the Lagrange multiplier on an edge $\Gamma^{e,e'}$—that is, constructing the space $\mathscr{W}^h$ with the approximate normal derivatives of u^E on the element edges while paying attention

DOI: 10.1002/nme

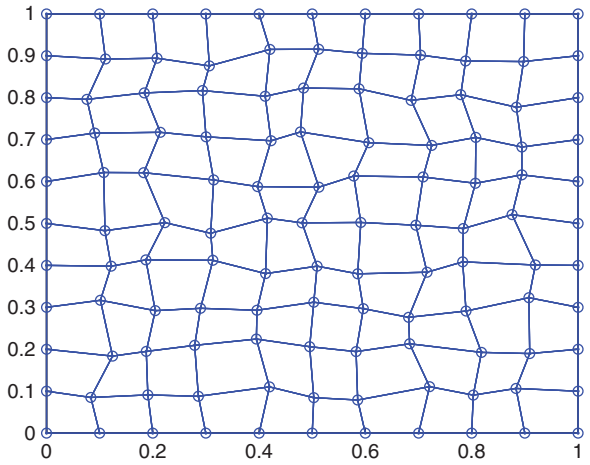

Figure 3. Sample unstructured mesh of 100 quadrilateral elements.

to not violating the Babuška–Brezzi *inf–sup* condition [33–35]. On a mesh of n_{el} quadrilateral elements, this condition implies the following asymptotic bound on the number of Lagrange multipliers per edge, n^{λ}:

$$n^{\lambda} \leqslant \frac{n^E}{2} \tag{30}$$

almost everywhere in the mesh. The bound (30) is a necessary, but in general *not* a sufficient condition for ensuring that a non-singular global interface problem arises in the application of DEM on a uniform mesh of square elements. In practice, fewer than $n^{\lambda} = n^E/2$ Lagrange multipliers per edge are used. Numerical tests [7] show that the general rule of thumb is to limit

$$n^{\lambda} = \left\lfloor \frac{n^E}{4} \right\rfloor \tag{31}$$

where, for any $x \in \mathbb{R}$, $\lfloor x \rfloor \equiv \max\{n \in \mathbb{Z} | n \leqslant x\}$—that is, $\lfloor \cdot \rfloor$ is the floor (or greatest integer) function.

In [7], the Lagrange multiplier approximations were derived assuming a uniform mesh of rectangular elements. In the present work that simplified formulation is extended to problems discretized on unstructured meshes of quadrilateral straight-edged elements (Figure 3).

Let $\Gamma^{ij} \equiv \Gamma^{e_i, e_j}$ be a straight edge separating two adjacent elements, Ω^{e_i} and Ω^{e_j}, viewed as an edge belonging to Ω^{e_i}. Let $\mathbf{x}_0^{ij} = (x_0^{ij}, y_0^{ij})$ and $\mathbf{x}_1^{ij} = (x_1^{ij}, y_1^{ij})$ be the coordinates of this edge, labeled with respect to a right-handed coordinate system so that the outward normal $\mathbf{n}^{ij}$ to Ω^{e_i} points to the right of Ω^{e_i} (Figure 4).

Let $\alpha^{ij} \in [0, \pi)$ be the angle Γ^{ij} makes with the x-axis and let l^{ij} be its length, defined by

$$\begin{aligned} \Delta x^{ij} &= l^{ij} \cos \alpha^{ij} \\ \Delta y^{ij} &= l^{ij} \sin \alpha^{ij} \end{aligned} \tag{32}$$

DOI: 10.1002/nme

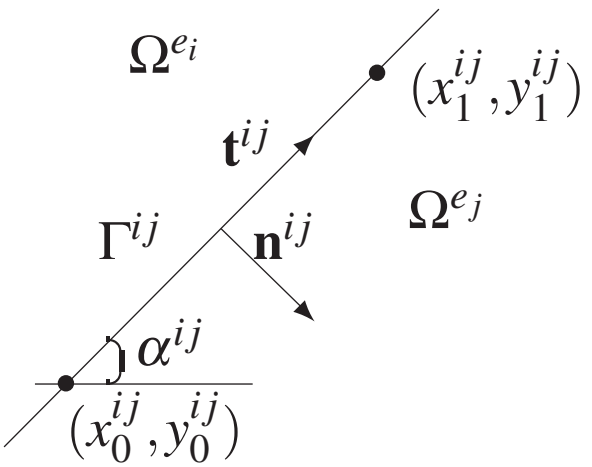

Figure 4. Straight edge of element Ω^{e_i} oriented at angle α^{ij}.

$$\Delta x^{ij} \equiv x_1^{ij} - x_0^{ij}, \quad \Delta y^{ij} \equiv y_1^{ij} - y_0^{ij} \tag{33}$$

$$l^{ij} = \sqrt{(\Delta x^{ij})^2 + (\Delta y^{ij})^2} \tag{34}$$

The unit tangent vector to Γ^{ij}, $\mathbf{t}^{ij}$, is given by

$$\mathbf{t}^{ij} = \frac{1}{l^{ij}} (\Delta x^{ij} \;\; \Delta y^{ij})^{\mathrm{T}} = (\cos\alpha^{ij} \;\; \sin\alpha^{ij})^{\mathrm{T}} \equiv (t_1^{ij} \;\; t_2^{ij})^{\mathrm{T}} \tag{35}$$

so that

$$\mathbf{n}^{ij} = (t_2^{ij} \;\; -t_1^{ij})^{\mathrm{T}} \tag{36}$$

Let $0 \leqslant s \leqslant l^{ij}$ denote the arc length coordinate. Γ^{ij} can be parameterized as follows:

$$\Gamma^{ij} : \begin{cases} x = x_0^{ij} + t_1^{ij} s \\ y = y_0^{ij} + t_2^{ij} s \end{cases}, \quad 0 \leqslant s \leqslant l^{ij} \tag{37}$$

As outlined in Section 3, the first step in designing a DGM or DEM element is to select the set Θ^u that defines the element's enrichment basis. Given the parametrization of Γ^{ij} (37) and the set Θ^u (24), one can begin by computing the corresponding Lagrange multiplier approximations according to (13)

$$\lambda^h(s)|_{\Gamma^{ij}} = \sum_{k=1}^{n^E} \lambda_k \underbrace{\exp\left\{\frac{1}{2}[(\mathbf{a}_\phi + \mathbf{a}_{\theta_k}) \cdot \mathbf{t}^{ij}](s - s_{r,k}^{ij})\right\}}_{\equiv \lambda^h(s;\theta_k)}, \quad 0 \leqslant s \leqslant l^{ij} \tag{38}$$

DOI: 10.1002/nme

where $\mathbf{t}^{ij}$ is the unit tangent vector to Γ^{ij} defined in (35), $s^{ij}_{r,k}$ is an arbitrary reference point and the λ_k are the unknown multiplier dofs. Substituting the expression of $\mathbf{t}^{ij}$ (35) in the above result and applying some trigonometric identities' transforms (38) into

$$\lambda^h(s)|_{\Gamma^{ij}} = \sum_{k=1}^{n^E} \lambda_k \underbrace{\exp\left\{\frac{|\mathbf{a}|}{2}[\cos(\phi-\alpha^{ij})+\cos(\theta_k-\alpha^{ij})](s-s^{ij}_{r,k})\right\}}_{\equiv\lambda^h(s;\theta_k)}, \quad 0\leqslant s\leqslant l^{ij} \tag{39}$$

This shows that $\lambda^h(s;\theta)|_{\Gamma^{ij}}$ is a function of Pe, ϕ (the advection direction), α^{ij} (the angle at which the edge Γ^{ij} is oriented) and $\theta_k \in \Theta^u$. In a uniform mesh aligned with the x- and y-coordinate axes, $\alpha^{ij}=0,\pi$ for the top/bottom edges of each element and $\alpha^{ij}=\pi/2,\ 3\pi/2$ for the left/right edges of each element. For these values, (39) recovers the formulas derived in [7] for the approximation of the Lagrange multiplier on the edges of a square element in a uniform mesh

$$\begin{aligned}
\lambda^{tb} &= \sum_{i=1}^{n^E} \lambda^{tb}_i \exp\left\{\frac{|\mathbf{a}|}{2}(\cos\phi+\cos\theta_i)(x-x_{r,i})\right\}, \quad x_j\leqslant x\leqslant x_{j+1}\\
\lambda^{lr} &= \sum_{i=1}^{n^E} \lambda^{lr}_i \exp\left\{\frac{|\mathbf{a}|}{2}(\sin\phi+\sin\theta_i)(y-y_{r,i})\right\}, \quad y_j\leqslant y\leqslant y_{j+1}
\end{aligned} \tag{40}$$

for an element $\Omega^e=(x_j,x_{j+1})\times(y_j,y_{j+1})\subset\mathbb{R}^2$. Here, λ^{tb} and λ^{lr} denote the Lagrange multiplier approximations on the top/bottom and left/right edges in the mesh, respectively.

The set Θ^u (24) typically leads to too many Lagrange multiplier dofs (38) in the sense that condition (30) fails. For this reason, the space of approximation of the Lagrange multiplier field is constructed as $\mathscr{W}^h=\cup_e\cup_{e_j<e_i}\mathscr{W}^h_{ij}$ where

$$\begin{aligned}
\mathscr{W}^h_{ij} = \Bigg\{ &\lambda^h\in L^2(\Gamma^{ij}) : \lambda^h(s)|_{\Gamma^{ij}} = \sum_{k=1}^{n^\lambda} \lambda_k \exp\left(\frac{1}{2}[(\mathbf{a}_\phi+\mathbf{a}_{\theta^\lambda_k})\cdot\mathbf{t}^{ij}](s-s^{ij}_{r,k})\right),\\
&0\leqslant s\leqslant l^{ij}, 0\leqslant\theta^\lambda_k<2\pi, \lambda_k\in\mathbb{R}\Bigg\}
\end{aligned} \tag{41}$$

Here, $\{\theta^\lambda_k\}_{k=1}^{n^\lambda}=\Theta^\lambda$ is another set of angles that is defined *a priori* and independently from Θ^u, and n^λ is the number of Lagrange multiplier dofs *per edge*.

Next, it is noted that a 'naïve' selection of the set Θ^λ defining $\mathscr{W}^h$ is likely to cause a Lagrange multiplier redundancy on some edge in the mesh. This is not desirable as it leads to a singularity in the algebraic system of equations associated with a discretization by DEM. For example, suppose $\Theta^\lambda=\{\theta^\lambda_1=0,\theta^\lambda_2=\pi\}$ and $\alpha^{ij}=\pi/2$ for a particular edge Γ^{ij}. Furthermore, suppose that the flow is advected from left to right so that $\phi=0$. Then, from (39) it follows that

$$\lambda^h|_{\Gamma^{ij}}(s;\theta^\lambda_1=0)=\lambda^h|_{\Gamma^{ij}}(s;\theta^\lambda_2=\pi)=1 \tag{42}$$

Hence, both angles $\theta^\lambda_1=0$ and $\theta^\lambda_2=\pi$ define the same constant Lagrange multiplier.

The following lemma defines a set of necessary conditions for the set Θ^λ to generate redundant Lagrange multiplier approximations. When $n^\lambda>2$, one must check that *each pair* of angles in the

DOI: 10.1002/nme

proposed set Θ^λ does not verify any of these conditions before finalizing the design of a DGM or DEM element.

Lemma 1
Two Lagrange multipliers $\lambda^h(s;\theta_1^\lambda)$ and $\lambda^h(s;\theta_2^\lambda)$ given by (38) (or equivalently (39)) on a straight edge Γ^{ij} parameterized by (37) are redundant (that is, $\lambda^h(s;\theta_1^\lambda)=C\lambda^h(s;\theta_2^\lambda)$ for some real constant C) if

$$\frac{\theta_1^\lambda-\theta_2^\lambda}{2}=n\pi \tag{43}$$

or

$$\frac{\theta_1^\lambda+\theta_2^\lambda}{2}=\alpha^{ij}+n\pi \tag{44}$$

for any $n\in\mathbb{Z}$, where α^{ij} is the angle at which Γ^{ij} is oriented (32).

Proof
From (39), $\lambda^h(s;\theta_1^\lambda)=\lambda^h(s;\theta_2^\lambda)$ if

$$\cos(\theta_1^\lambda-\alpha^{ij})=\cos(\theta_2^\lambda-\alpha^{ij}) \tag{45}$$

Clearly (45) holds if $\theta_1^\lambda=\theta_2^\lambda+2n\pi$ for any $n\in\mathbb{Z}$, which proves (43). Since $\cos(\cdot)$ is even, (45) is equivalent to

$$\cos(\theta_1^\lambda-\alpha^{ij})=\cos(\alpha^{ij}-\theta_2^\lambda) \tag{46}$$

which holds if $\theta_1^\lambda-\alpha^{ij}=\alpha^{ij}-\theta_2^\lambda+2n\pi$ or $\frac{\theta_1^\lambda+\theta_2^\lambda}{2}=\alpha^{ij}+n\pi$ for $n\in\mathbb{Z}$. □

5. GENERAL AND MESH INDEPENDENT ELEMENT DESIGN PROCEDURE

A general procedure for designing a DGM or DEM element with an enrichment space containing n^E basis functions is summarized in Algorithm 1.

Condition (44) of Lemma 1 motivates choosing Θ^λ as a set of angles that are clustered around α^{ij}—that is,

$$\Theta^\lambda=\alpha^{ij}+\{\beta_k^\lambda\}_{k=1}^{n^\lambda},\quad \{\beta_k^\lambda\}_{k=1}^{n^\lambda}\in[0,2\pi) \tag{47}$$

in which case (39) simplifies to

$$\lambda^h(s)|_{\Gamma^{ij}}=\sum_{k=1}^{n^\lambda}\lambda_k\exp\left(\frac{|\mathbf{a}|}{2}[\cos(\phi-\alpha^{ij})+\cos\beta_k^\lambda](s-s_{r,k})\right) \tag{48}$$

for $0\leqslant s\leqslant l^{ij}$. For the choice of angles (47), the necessary condition for redundancy (44) becomes

$$\frac{\theta_k^\lambda+\theta_l^\lambda}{2}=\alpha^{ij}+n\pi\Leftrightarrow\frac{\beta_k^\lambda+\beta_l^\lambda}{2}=n\pi \tag{49}$$

DOI: 10.1002/nme

Algorithm 1 DGM/DEM element design

Fix $n^E \in \mathbb{N}$, the desired number of angles defining the enrichment space $\mathcal{V}^E$ (23).
Select a set $\Theta^u = \phi + \{\theta_i\}_{i=1}^{n^E}$ of n^E distinct angles between $[0, 2\pi)$ for which no pair of angles satisfy any of the conditions stated in Lemma 4.1, and which:
if designing a pure DGM element **then**
  Includes $\theta_i = \phi - \pi$ in Θ^u
else
  Omits $\theta_i = \phi - \pi$ from Θ^u.
end if
Let $n^\lambda = \lfloor \frac{n^E}{4} \rfloor$.
Choose a set of n^λ distinct angles $\{\beta_k\}_{k=1}^{n^\lambda}$ between $[0, \pi)$.
for each edge $\Gamma^{ij} \in \Gamma^{\text{int}}$ having slope α^{ij} **do**
  Let $\Theta^\lambda = \alpha^{ij} + \{\beta_k\}_{k=1}^{n^\lambda}$ be the set of angles defining the Lagrange multiplier approximations (41) on $\Gamma^{e,e'}$.
end for

for any two distinct $k, l \in \{1, 2, \ldots, n^\lambda\}$. Since condition (49) is independent of α^{ij}, condition (44) is in this case (quadrilateral) mesh independent.

A consequence of the element design approach outlined in Algorithm 1 is that, in general,

$$\Theta^\lambda \not\subset \Theta^u \tag{50}$$

Selecting Θ^λ independently of Θ^u is actually rather intuitive: since there are almost always more normal derivatives of the enrichment functions in $\mathscr{V}^E$ than allowed by (31) and one does not know *a priori* which of these Lagrange multipliers are more important and should be kept in Θ^λ, and which are less important and can be omitted, a reasonable compromise is to define Θ^λ as some average of the angles in Θ^u. Indeed, in practice, the angles $\{\beta_k^\lambda\}_{k=1}^{n^\lambda}$ that define the set Θ^λ (47) are selected uniformly between the angles $[0, \pi)$ so as to 'cover' the $\mathbb{R}^2$ space in some way (Table III).

6. HIGHER-ORDER 2D DGM AND DEM ELEMENTS FOR ADVECTION–DIFFUSION

Here, several higher-order quadrilateral DGM and DEM elements are proposed for the finite element solution of 2D advection–diffusion problems on unstructured meshes. The notation used for describing these elements is summarized in Table II. The letter 'Q' stands for 'quadrilateral'. As before, n^E denotes the number of enrichment functions (number of angles in the set Θ^u) and n^λ the number of Lagrange multiplier dofs per edge (number of angles in the set Θ^λ). Two cases are distinguished: $Pe \leqslant 10^3$ (small to moderate Péclet number regime), and $Pe > 10^3$ (high Péclet number regime). In the latter case, the DGM and DEM elements are designed slightly differently to address some numerical issues and distinguished by the presence of a horizontal bar over their names ($\overline{\cdot - \cdot - \cdot}$). The '+' superscript designates a genuine DEM element ($u^h = u^P + u^E$) and distinguishes it from a DGM element ($u^h = u^E$).

DOI: 10.1002/nme

Since the approximation space $\mathscr{V}^E$ is constructed independently from $\mathscr{V}^P$, the polynomial component of a DEM element can be set to that of any higher-order standard Galerkin element Q_p, independently from the value of n^E. From a practical perspective, it is however unnecessary to do so because for most advection–diffusion problems, the benefit of including a higher-order polynomial approximation in a DEM element is already provided by the presence of the enrichment field in this element. For this reason and in order to maximize computational efficiency, all DEM elements described in this section share the same low-order polynomial component that is identical to that of the standard bilinear element Q_1. Hence,

$$Q-n^E-n^{\lambda+}\equiv[Q-n^E-n^\lambda]\cup[Q_1],\quad \overline{Q-n^E-n^{\lambda+}}\equiv[\overline{Q-n^E-n^\lambda}]\cup[Q_1] \tag{51}$$

6.1. Element design for $Pe\leqslant 10^3$

Table III describes three DGM elements and three DEM elements designed according to the general procedure outlined in Section 5. For all these elements, the enrichment bases are defined by

$$\Theta^u=\{\theta_{m+1}\}_{m=0}^{n^E-1}\equiv\phi+\{\beta_{m+1}\}_{m=0}^{n^E-1},\quad \beta_m=\frac{2m\pi}{n^E} \tag{52}$$

Note in Table III that for all DEM elements, n^E is chosen as an odd integer. This ensures that $\theta_i=n\phi-\pi$, $n\in\mathbb{Z}$, is *not* included in Θ^u and therefore the constant approximation is not included in this case in the enrichment field. Note also that all values of n^λ are specified according to (31), all sets Θ^λ defining the Lagrange multiplier approximations have the form (47), and all sets $\{\beta_k\}_{k=1}^{n^\lambda}$ are such that condition (49) is avoided by all pairs of angles in these sets.

As an example, the DGM element $Q-8-2$ described in Table III is graphically depicted in Figure 5.

Table II. Notation.

Element	$Pe\leqslant 10^3$	$Pe>10^3$
DGM	$Q-n^E-n^\lambda$	$\overline{Q-n^E-n^\lambda}$
DEM	$Q-n^E-n^{\lambda+}$	$\overline{Q-n^E-n^{\lambda+}}$

Table III. Higher-order DGM and DEM elements.

	Name	n^E	Θ^u	n^λ	Θ^λ
DGM element	$Q-8-2$	8	$\phi+\{\frac{m\pi}{4}:m=0,\ldots,7\}$	2	$\alpha^{ij}+\{0,\frac{\pi}{2}\}$
	$Q-12-3$	12	$\phi+\{\frac{m\pi}{6}:m=0,\ldots,11\}$	3	$\alpha^{ij}+\{\frac{\pi}{4},\frac{\pi}{2},\frac{3\pi}{4}\}$
	$Q-16-4$	16	$\phi+\{\frac{m\pi}{8}:m=0,\ldots,15\}$	4	$\alpha^{ij}+\{0,\frac{\pi}{4},\frac{\pi}{2},\frac{3\pi}{4}\}$
DEM element	$Q-9-2^+$	9	$\phi+\{\frac{2m\pi}{9}:m=0,\ldots,8\}$	2	$\alpha^{ij}+\{0,\frac{\pi}{2}\}$
	$Q-13-3^+$	13	$\phi+\{\frac{2m\pi}{13}:m=0,\ldots,12\}$	3	$\alpha^{ij}+\{\frac{\pi}{4},\frac{\pi}{2},\frac{3\pi}{4}\}$
	$Q-17-4^+$	17	$\phi+\{\frac{2m\pi}{17}:m=0,\ldots,16\}$	4	$\alpha^{ij}+\{0,\frac{\pi}{4},\frac{\pi}{2},\frac{3\pi}{4}\}$

DOI: 10.1002/nme

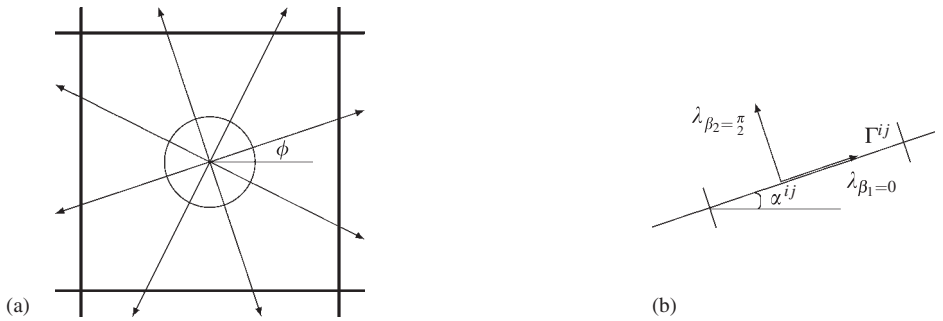

Figure 5. Illustration of the sets Θ and Θ^{λ} that define the $Q-8-2$ element. (a) Enrichment basis and (b) Lagrange multiplier dofs.

6.2. *Element design for* $Pe>10^3$

A difficulty arises in the implementation of the elements described in Section 6.1 when the Péclet number is very large, say $Pe>10^3$. Such a Péclet number can be encountered in high Reynolds number flows. In this case, it is found that even with the use of a reference point $\mathbf{x}^e_{r,i}$ inside each element Ω^e (see Section 7.3), the local and global matrices arising from the DGM or DEM discretizations become ill-conditioned. To address this issue, 'advection-limited' variants of the DGM and DEM elements described so far are designed to operate in the high Péclet number regime defined here as $Pe>10^3$. In these variant elements, the advection coefficients appearing in the arguments of the exponential functions of the enrichment basis are limited to an experimentally determined 'safe' value of 10^3 to obtain approximation

$$\overline{u}^E(\mathbf{x};\phi)|_{\Omega^e}=\sum_{i=1}^{n^E}\exp\left\{\frac{1}{2}(\mathbf{a}_\phi+\overline{\mathbf{a}}_{\theta_i})\cdot(\mathbf{x}-\mathbf{x}^e_{r,i})\right\},\quad \overline{\mathbf{a}}^{\mathrm{T}}_{\theta_i}\equiv\min\{10^3,|\mathbf{a}|\}(\cos\theta_i\quad\sin\theta_i) \tag{53}$$

where the bar notation is used to designate advection limitation. The resulting DGM and DEM elements are denoted by $\overline{Q-n^E-n^{\lambda}}$ (DGM) and $\overline{Q-n^E-n^{\lambda+}}$ (DEM).

It is noted that for $Pe>10^3$, functions of the form (53) are not free-space solutions of the homogeneous advection–diffusion equation for the original Péclet number. Instead, they are free-space solutions of the homogeneous advection–diffusion equations for *different* and lower Péclet numbers. Nevertheless, these functions are more pertinent to the problem of interest than mere polynomials.

7. IMPLEMENTATION AND COMPUTATIONAL PROPERTIES

The discretization of equations (9) by DEM as described in Section 3 gives rise to the following matrix problem:

$$\begin{pmatrix}\mathbf{k}^{\mathrm{PP}} & \mathbf{k}^{\mathrm{PE}} & \mathbf{k}^{\mathrm{PC}}\\ \mathbf{k}^{\mathrm{EP}} & \mathbf{k}^{\mathrm{EE}} & \mathbf{k}^{\mathrm{EC}}\\ \mathbf{k}^{\mathrm{CP}} & \mathbf{k}^{\mathrm{CE}} & \mathbf{0}\end{pmatrix}\begin{pmatrix}\mathbf{u}^{\mathrm{P}}\\ \mathbf{u}^{\mathrm{E}}\\ \boldsymbol{\lambda}\end{pmatrix}=\begin{pmatrix}\mathbf{r}^{\mathrm{P}}\\ \mathbf{r}^{\mathrm{E}}\\ \mathbf{r}^{\mathrm{C}}\end{pmatrix} \tag{54}$$

DOI: 10.1002/nme

where $\mathbf{u}^{\mathrm{E}}$, $\mathbf{u}^{\mathrm{P}}$ and $\boldsymbol{\lambda}$ are vectors containing the dofs u^E, u^P and λ^h, respectively. The superscript 'C' refers to the continuity constraints enforced weakly by the Lagrange multipliers. $\mathbf{k}^{\mathrm{EE}}$, $\mathbf{k}^{\mathrm{EP}}$ and $\mathbf{k}^{\mathrm{PP}}$ are associated with the bilinear forms $a(v^E, u^E)$, $a(v^E, u^P)$ and $a(v^P, u^P)$ (10), respectively; $\mathbf{k}^{\mathrm{EC}}$ and $\mathbf{k}^{\mathrm{PC}}$ are associated with $b(v^E, \lambda^h)$ and $b(v^P, \lambda^h)$ (11), respectively; $\mathbf{r}^{\mathrm{E}}$ and $\mathbf{r}^{\mathbf{P}}$ are associated with $r(v^E)$ and $r(v^P)$ (12), respectively; $\mathbf{r}^{\mathrm{C}}$ is associated with $r_d(\lambda^h)$ (12).

Owing to the discontinuous nature of $\mathscr{V}^E$, u^E can be eliminated at the element level by a static condensation. For a DEM element, forming the Schur complement of the second equation in (54) and substituting this expression into the first and third equations leads to the following (local) statically condensed system:

$$\begin{pmatrix} \tilde{\mathbf{k}}^{\mathrm{PP}} & \tilde{\mathbf{k}}^{\mathrm{PC}} \\ \tilde{\mathbf{k}}^{\mathrm{CP}} & \tilde{\mathbf{k}}^{\mathrm{CC}} \end{pmatrix} \begin{pmatrix} \mathbf{u}^{\mathrm{P}} \\ \boldsymbol{\lambda} \end{pmatrix} = \begin{pmatrix} \tilde{\mathbf{r}}^{\mathrm{P}} \\ \tilde{\mathbf{r}}^{\mathrm{C}} \end{pmatrix} \tag{55}$$

where

$$\begin{aligned} \tilde{\mathbf{k}}^{\mathrm{PP}} &= \mathbf{k}^{\mathrm{PP}} - \mathbf{k}^{\mathrm{PE}}(\mathbf{k}^{\mathrm{EE}})^{-1}\mathbf{k}^{\mathrm{EP}} \\ \tilde{\mathbf{k}}^{\mathrm{PC}} &= \mathbf{k}^{\mathrm{PC}} - \mathbf{k}^{\mathrm{PE}}(\mathbf{k}^{\mathrm{EE}})^{-1}\mathbf{k}^{\mathrm{EC}} \\ \tilde{\mathbf{k}}^{\mathrm{CP}} &= \mathbf{k}^{\mathrm{CP}} - \mathbf{k}^{\mathrm{CE}}(\mathbf{k}^{\mathrm{EE}})^{-1}\mathbf{k}^{\mathrm{EP}} \\ \tilde{\mathbf{k}}^{\mathrm{CC}} &= -\mathbf{k}^{\mathrm{CE}}(\mathbf{k}^{\mathrm{EE}})^{-1}\mathbf{k}^{\mathrm{EC}} \end{aligned} \tag{56}$$

and

$$\begin{aligned} \tilde{\mathbf{r}}^{\mathrm{P}} &= \mathbf{r}^{\mathrm{P}} - \mathbf{k}^{\mathrm{PE}}(\mathbf{k}^{\mathrm{EE}})^{-1}\mathbf{r}^{\mathrm{E}} \\ \tilde{\mathbf{r}}^{\mathrm{C}} &= \mathbf{r}^{\mathrm{C}} - \mathbf{k}^{\mathrm{CE}}(\mathbf{k}^{\mathrm{EE}})^{-1}\mathbf{r}^{\mathrm{E}} \end{aligned} \tag{57}$$

In the case of a DGM element, there is no polynomial field and therefore $\tilde{\mathbf{k}}^{\mathrm{PP}}$, $\tilde{\mathbf{k}}^{\mathrm{PC}}$, $\tilde{\mathbf{k}}^{\mathrm{CP}}$, $\tilde{\mathbf{r}}^{\mathrm{P}} = \{\emptyset\}$, and the statically condensed system simplifies to

$$-\mathbf{k}^{\mathrm{CE}}(\mathbf{k}^{\mathrm{EE}})^{-1}\mathbf{k}^{\mathrm{EC}}\boldsymbol{\lambda} = \mathbf{r}^{C} - \mathbf{k}^{\mathrm{CE}}(\mathbf{k}^{\mathrm{EE}})^{-1}\mathbf{r}^{\mathrm{E}} \tag{58}$$

7.1. Computational complexity

One computational advantage of DEM is that its computational complexity is not directly determined by the dimension of $\mathscr{V}^E$. Instead, it depends on the total number of Lagrange multiplier dofs and the sparsity pattern of the system matrix (55) (DEM) or (58) (DGM). This property is a result of the element-level static condensation (55), which is enabled by the discontinuous nature of the approximation of the solution.

The computational complexities of the DGM and DEM elements proposed in Section 6 are given in Table IV for the case of a mesh of $n_{el} = n^2$ quadrilateral elements. For reference, the table also includes the computational complexity of each of the standard 2D Lagrangian biquadratic, bicubic and biquartic quadrilateral Galerkin elements, denoted here by Q_2, Q_3 and Q_4, respectively. Roughly speaking, one can say that two elements within the same following pairs or triplets have comparable computational complexities: $(Q-8-2, Q-9-2^+, Q_2)$, $(Q-12-3, Q-13-3^+, Q_3)$ and $(Q-16-4, Q-17-4^+, Q_4)$.

Also reported in Table IV is the stencil width of each element for an $n \times n$ uniform mesh, a measure of the sparsity pattern of the resulting system matrix. The reader can observe that

DOI: 10.1002/nme

Table IV. Computational complexity of some DGM, DEM and standard Galerkin elements.

Element	Asymptotic # of dofs	Stencil width for uniform $n \times n$ mesh
Q_2	$3n_{el}$	21
Q_3	$5n_{el}$	33
Q_4	$7n_{el}$	45
$Q-8-2$	$4n_{el}$	14
$Q-12-3$	$6n_{el}$	21
$Q-16-4$	$8n_{el}$	28
$Q-9-2^+$	$5n_{el}$	33
$Q-13-3^+$	$7n_{el}$	45
$Q-17-4^+$	$9n_{el}$	57

the stencil of a DGM discretization is smaller than that of the Galerkin element that leads to a comparable total number of dofs for a given problem.

7.2. Analytical computation of element level arrays

A convenient property of the enrichment basis (23) is that (10)–(12) can be integrated analytically on any mesh of quadrilateral straight-edged elements. For example, let $\mathbf{k}^{\mathrm{EC}}_{km}|_{\Gamma^{ij}}$ be the (k,m) component of the $\mathbf{k}^{\mathrm{EC}}$ matrix on the edge Γ^{ij} having slope α^{ij} and length l^{ij}. Using the notation introduced in Section 3,

$$\begin{aligned}\mathbf{k}^{\mathrm{EC}}_{km}|_{\Gamma^{ij}} &= \int_0^{l^{ij}} u^E(\mathbf{x};\theta_k)|_{\Gamma^{ij}} \lambda^h(s;\theta_m)\,\mathrm{d}s \\ &= \int_0^{l^{ij}} \exp\left\{\frac{1}{2l^{ij}}(2\mathbf{a}_\phi + \mathbf{a}_{\theta_k} + \mathbf{a}_{\theta_m})\cdot\Delta\mathbf{x}^{ij}s - r_u(\theta_k) - r_\lambda(\theta_m)\right\}\mathrm{d}s \end{aligned} \tag{59}$$

where

$$r_u(\theta_k) \equiv \frac{1}{2}(\mathbf{a}_\phi + \mathbf{a}_{\theta_k})\cdot(\mathbf{x}^e_{r,k} - \mathbf{x}^{ij}_0), \quad r_\lambda(\theta_m) \equiv \frac{1}{2l^{ij}}(\mathbf{a}_\phi + \mathbf{a}_{\theta_m})\cdot(\Delta\mathbf{x}^{ij}s^{ij}_{r,m}) \tag{60}$$

The integral (59) is a simple one-dimensional integral of an exponential function. Similarly, all other integrations incurred by the element level matrices and vectors simplify to integrals of exponentials. These can be evaluated analytically, thereby eliminating the need for any quadrature rule and avoiding the associated numerical errors.

Another convenient property of the functions (23) is that they satisfy $\mathscr{L}u^E = 0$. As a result, integration by parts of (10) gives

$$a(v^E, u^E) = \int_{\tilde{\Omega}} (\nabla v^E \cdot \nabla u^E + \mathbf{a}\cdot\nabla u^E v^E)\,\mathrm{d}\Omega = \int_{\tilde{\Gamma}} \nabla u^E \cdot \mathbf{n} v^E\,\mathrm{d}\Gamma \tag{61}$$

Thus, no volume integral involving the exponential enrichments needs be computed, which further simplifies the implementation of a DGM or DEM element.

DOI: 10.1002/nme

7.3. Reference point

As mentioned earlier, the enrichment functions (23) are scaled by the effect of an arbitrary reference point $\mathbf{x}^e_{r,i}$ within each element Ω^e to avoid evaluating a very large floating point number on a finite precision arithmetic processor. Numerical experiments demonstrate that overflow is inevitable if the same reference point is used for each of the enrichment functions. The following algorithm for setting the reference points produces good performance for the DGM and DEM elements proposed herein.

In Algorithm 2, $\mathbf{a}_\phi$ and $\mathbf{a}_{\theta_i}$ are defined in (22), $\mathbf{a}_\phi(j)$ ($\mathbf{a}_\theta(j)$), $j=1,2$, is the jth component of $\mathbf{a}_\phi$ ($\mathbf{a}_\theta$), and $\{(x^e_k, y^e_k)\}^4_{k=1}$ are the coordinates of the nodes of element Ω^e. An analogous algorithm is used to determine the Lagrange multiplier reference points $s^{ij}_{r,k}$ which are set either to 0 or to l^{ij} depending on the sign of the argument of the exponential in (41).

Algorithm 2 Selection of enrichment function reference point

```
for j = 1 to n_el do
  for i = 1 to n^E do
    if a_φ(1) + a_θi(1) ⩾ 0 then
      x^e_{r,i} = max{x^e_k}^4_{k=1}
    else
      x^e_{r,i} = min{x^e_k}^4_{k=1}
    end if
    if a_φ(2) + a_θi(2) ⩾ 0 then
      y^e_{r,i} = max{y^e_k}^4_{k=1}
    else
      y^e_{r,i} = min{y^e_k}^4_{k=1}
    end if
  end for
end for
```

8. NUMERICAL RESULTS

Here, the higher-order DGM and DEM advection–diffusion elements described in Section 6 are tested on four benchmark problems:

(i) A homogeneous boundary layer problem on the unit square whose exact solution is spanned by the DGM basis (23) [Section 8.1].
(ii) A homogeneous boundary layer problem on the unit square whose exact solution is *not* spanned by the DGM basis (23) [Section 8.2].
(iii) A two-scale inhomogeneous BVP on the unit square [Section 8.3].
(iv) A 'double ramp' problem on an L-shaped domain [Section 8.4].

In each case, the performance of the DGM and/or DEM elements of Section 6 is contrasted with that of standard Galerkin elements. For the first benchmark problem (Section 8.1), it is also compared with that of several stabilized finite elements developed in [36], as these elements were also tested by their developers on this problem. It is emphasized that all elements denoted by

DOI: 10.1002/nme

Q_n, $n=1,2,3,4$, are *non-stabilized* Galerkin elements. All reported errors are relative errors measured in the $L^2(\Omega)$ 'broken' norm. For a DGM element with n^E enrichment functions, the absolute counterpart of this error $\mathscr{E}$ is computed as follows:

$$\mathscr{E}^2=\sum_e \left\| \sum_{i=1}^{n^E} d_i u^E(\mathbf{x};\theta_i)|_{\Omega^e} - u_{\text{ref}}(\mathbf{x})|_{\Omega^e} \right\|^2_{L^2(\Omega^e)} = \sum_e \left\{ \int_{\Omega^e} \left(\sum_{i=1}^{n^E} d_i u^E(\mathbf{x};\theta_i) - u_{\text{ref}}(\mathbf{x}) \right)^2 \mathrm{d}\Omega \right\} \quad (62)$$

where $u_{\text{ref}}(\mathbf{x})$ is a reference (or the exact) solution, $u^E(\mathbf{x};\theta_i)$ are the enrichment functions given by (21), and d_i are the enrichment dofs. The errors are measured either with respect to the exact solution (when available, as in the case of problems (i)–(iii)), or a reference solution computed using a sufficiently refined mesh (problem (iv)). All comparisons are performed between elements of similar computational complexity *a priori*, either for a specified level of accuracy or for a fixed total number of dof. It turns out that all compared elements have also a similar convergence rate *a posteriori*.

All unstructured meshes are generated by perturbing the nodes of an $n\times n$ uniform mesh (see e.g. Figure 3). All integrals (10)–(12) and therefore all matrices and right-hand sides (54) are computed exactly.

8.1. Homogeneous boundary layer problem with a flow aligned with the advection direction

Let $\Omega=(0,1)\times(0,1)$. Consider the BVP (1) with $f=0$ and Dirichlet boundary conditions on Γ designed so that the exact solution of this problem is

$$u_{ex}(\mathbf{x};\phi)=\frac{e^{\mathbf{a}_\phi\cdot(\mathbf{x}-\mathbf{1})}-1}{e^{-\mathbf{a}_\phi\cdot\mathbf{1}}-1} \quad (63)$$

where $\mathbf{1}^{\mathrm{T}}\equiv(1\ \ 1)$ and $\mathbf{a}_\phi$ is defined in (22). Since the length of the domain is equal to one, the global Péclet number on Ω is given by $Pe=|\mathbf{a}|$. For a specified advection direction ϕ and Péclet number Pe, the solution of this BVP exhibits a boundary layer in the direction ϕ whose gradient is a function of Pe. The higher is Pe, the steeper is the solution.

Among all elements developed in Section 6, only the pure DGM elements $Q-8-2$, $Q-12-3$ and $Q-16-4$ are considered for the solution of this benchmark problem because it is a homogeneous one. In addition, the lower-order DGM element $Q-4-1$, which is an extension to unstructured quadrilaterals based on the approach outlined in Section 4 of the rectangular DGM element $R-4-1$ previously developed in [7], is applied to the solution of this BVP. Element $Q-4-1$ is characterized by the sets of angles

$$\Theta^u_{Q-4-1}=\phi+\left\{\frac{m\pi}{2}:m=0,\ldots,3\right\},\quad \Theta^\lambda_{Q-4-1}=\{\phi\} \quad (64)$$

The performance results obtained for these DGM elements are compared with those of several standard Galerkin and stabilized finite elements when the size of the problem is kept fixed at approximately 400 dofs. Before commenting on these results, it is noted that:

- For this BVP, $u_{ex}\in\mathscr{V}^E$ for all DGM elements considered herein and all advection directions ϕ. However, this does not mean that each of these DGM elements should be expected to recover the exact solution (63), *unless* $\nabla u_{ex}\cdot\mathbf{n}\in\mathscr{W}^h$ of this element.

DOI: 10.1002/nme

- For a uniform discretization, α^{ij} (Figure 4) takes the values of $0, \pi/2, \pi$ or $3\pi/2$ for all edges $\Gamma^{ij} \in \Gamma^{\text{int}}$ of the mesh. From Table III and the information given in (64), it follows that in this case, for each considered DGM element, $\nabla u_{ex} \cdot \mathbf{n} \in \mathscr{W}^h$ for the advection directions given in Table V.
- Therefore, for $\phi = 0$, all four DGM elements considered herein should capture the solution of the BVP defined above to machine precision. For $\phi = \pi/6$, only the $Q-4-1$ element should do so. For $\phi = \pi/4$, all four DGM elements considered herein except $Q-8-2$ should capture the exact solution to machine precision.

Table VI reports for $Pe = 10^2$ and $Pe = 10^3$ and three different advection directions the relative errors associated with the solutions computed on uniform meshes using the standard Galerkin element Q_1, three different stabilized versions of this bilinear element developed in [36] under the labels STR, EST and FFH, and the lower-order DGM element $Q-4-1$ that has a comparable complexity. In all cases, the number of dofs is kept fixed at about 400. The reader can observe that, consistently with the remarks formulated above, the DGM element $Q-4-1$ reproduces the exact solution to almost machine precision for all three advection directions $\phi = 0$, $\phi = \pi/6$ and $\phi = \pi/4$. As such, it outperforms in these cases—by a large margin—the standard Galerkin element Q_1 and all of its considered stabilized counterparts.

Similarly, Table VII reports the relative errors associated with the numerical solutions provided by the elements Q_1, STR, EST, FFH, and the advection-limited DGM element $Q-4-1$, for the

Table V. Advection directions $\phi/\pi \in \{0, 1/6, 1/4\}$ for which $\nabla u_{ex} \cdot \mathbf{n} \in \mathscr{W}^h$ for uniform discretizations of Ω (Section 8.1).

	ϕ/π		
DGM element	0	$\frac{1}{6}$	$\frac{1}{4}$
$\nabla u_{ex} \cdot \mathbf{n} \in \mathscr{W}^h$?			
$Q-4-1$	✓	✓	✓
$Q-8-2$	✓		
$Q-12-3$	✓		✓
$Q-16-4$	✓		✓

Table VI. Homogeneous boundary layer problem of Section 8.1 with $Pe \leqslant 10^3$: relative errors in the $L^2(\Omega)$ broken norm for uniform discretizations with approximately 400 dofs (non-stabilized and stabilized Galerkin Q_1 elements vs DGM $Q-4-1$ element).

Pe	ϕ/π	Q_1	STR	EST	FFH	$Q-4-1$
10^2	0	8.97×10^{-2}	7.62×10^{-2}	7.62×10^{-2}	8.59×10^{-2}	3.06×10^{-15}
	$\frac{1}{6}$	1.31×10^{-2}	1.14×10^{-2}	1.15×10^{-2}	1.25×10^{-2}	1.18×10^{-16}
	$\frac{1}{4}$	1.31×10^{-2}	1.14×10^{-2}	1.15×10^{-2}	1.26×10^{-2}	2.66×10^{-15}
10^3	0	5.77×10^{-1}	1.28×10^{-1}	1.28×10^{-1}	1.29×10^{-2}	3.43×10^{-14}
	$\frac{1}{6}$	2.53×10^{-2}	1.67×10^{-2}	1.67×10^{-2}	1.75×10^{-2}	1.24×10^{-15}
	$\frac{1}{4}$	2.62×10^{-2}	1.67×10^{-2}	1.67×10^{-2}	1.77×10^{-2}	3.19×10^{-14}

DOI: 10.1002/nme

Table VII. Homogeneous boundary layer problem of Section 8.1 with $Pe=10^6$: relative errors in the $L^2(\Omega)$ broken norm for uniform discretizations with approximately 400 dofs (non-stabilized and stabilized Galerkin Q_1 elements vs advection-limited DGM $\overline{Q-4-1}$ element).

Pe	ϕ/π	Q_1	STR	EST	FFH	$\overline{Q-4-1}$
10^6	0	8.44×10^{2}	1.29×10^{-1}	1.29×10^{-1}	1.29×10^{-1}	2.24×10^{-2}
	$\frac{1}{6}$	9.75	1.67×10^{-2}	1.67×10^{-2}	1.75×10^{-2}	1.11×10^{-3}
	$\frac{1}{4}$	9.97	1.67×10^{-2}	1.67×10^{-2}	1.67×10^{-2}	1.29×10^{-3}

case of the very large Péclet number of 10^6. The solutions provided by the considered stabilized finite elements are shown to be on average about four orders of magnitude more accurate for $\phi=0$ and three orders of magnitude more accurate for $\phi\neq0$ than that generated by the standard element Q_1. Since by construction, the basis functions of advection-limited DGM elements are not free-space solutions of the homogeneous advection–diffusion equation for the original Péclet number, the DGM element $\overline{Q-4-1}$ cannot capture the exact solution to almost machine precision. However, at least for this benchmark problem, this element is found to deliver a numerical solution that is about one order of magnitude more accurate than that delivered by any of the considered stabilized finite element.

Table VIII reports for $Pe=10^2$ and $Pe=10^3$ and the same three different advection directions as before the relative errors associated with the solutions computed on uniform meshes using the standard Galerkin elements Q_2, Q_3 and Q_4, and the higher-order DGM elements $Q-8-2$, $Q-12-3$ and $Q-16-4$. In all cases, the number of dofs is kept fixed at 400. For $\phi=0$, the DGM element $Q-8-2$ performs as expected and captures the exact solution of the BVP considered herein to almost machine precision. In the other two cases, this element whose computational complexity is similar to that of the standard Galerkin element Q_2 produces numerical solutions that are one order of magnitude more accurate than those delivered by the Q_2 element when $Pe=10^2$, and one to four orders of magnitude more accurate when $Pe=10^3$. Similarly, the DGM element $Q-12-3$ captures as expected the exact solution to almost machine precision for $\phi=0$ and $\phi=\pi/4$. For $\phi=\pi/6$, this element whose computational complexity is comparable to that of element Q_3 produces a numerical solution that is two orders of magnitude more accurate than that delivered by the element Q_3 when $Pe=10^2$, and almost four orders of magnitude more accurate when $Pe=10^3$. Similar conclusions can be drawn from the comparison of the performances of the DGM element $Q-16-4$ and the standard Galerkin element Q_4 for the solution of this BVP problem on structured meshes using 400 dofs.

On unstructured meshes, a DEM or DGM element whose enrichment field happens to include the exact solution of the problem of interest cannot be expected to capture that exact solution to machine precision at low mesh resolution because even in this case, $\nabla u_{ex}\cdot\mathbf{n}\notin\mathscr{W}^h$ in general. However, the performance results reported in Table IX show that in this case, the DGM methodology outperforms the standard Galerkin methodology by a large margin. More specifically, for the solution on unstructured meshes using a fixed number of 400 dofs of the BVP considered herein with $Pe=10^2$ and $Pe=10^3$, the DGM element $Q-8-2$ is found to deliver numerical results that are one to three orders of magnitude more accurate than those delivered by the element Q_2. The relative errors associated with the solutions produced by the $Q-12-3$ element are shown to be two to five orders of magnitude smaller than those associated with the numerical solutions computed with the element Q_3, and those associated with the solutions computed using the element $Q-16-4$

DOI: 10.1002/nme

Table VIII. Homogeneous boundary layer problem of Section 8.1 with $Pe \leqslant 10^3$: relative errors in the $L^2(\Omega)$ broken norm for uniform discretizations with approximately 400 dofs (non-stabilized Galerkin vs DGM elements).

Pe	ϕ/π	Q_2	$Q-8-2$	Q_3	$Q-12-3$	Q_4	$Q-16-4$
10^2	0	5.77×10^{-2}	4.77×10^{-15}	4.06×10^{-2}	8.03×10^{-14}	2.39×10^{-2}	9.22×10^{-13}
	$\frac{1}{6}$	6.52×10^{-3}	2.40×10^{-4}	3.95×10^{-3}	6.61×10^{-5}	2.02×10^{-3}	1.03×10^{-5}
	$\frac{1}{4}$	6.51×10^{-3}	2.67×10^{-4}	3.83×10^{-3}	1.22×10^{-14}	1.87×10^{-3}	4.56×10^{-13}
10^3	0	4.33×10^{-1}	2.22×10^{-10}	3.68×10^{-1}	5.78×10^{-13}	2.44×10^{-1}	9.75×10^{-10}
	$\frac{1}{6}$	1.49×10^{-2}	8.38×10^{-4}	1.21×10^{-2}	5.50×10^{-6}	9.47×10^{-3}	3.31×10^{-6}
	$\frac{1}{4}$	1.53×10^{-2}	5.62×10^{-6}	1.24×10^{-2}	4.36×10^{-14}	9.81×10^{-3}	1.27×10^{-12}

Table IX. Homogeneous boundary layer problem of Section 8.1 with $Pe \leqslant 10^3$: relative errors in the $L^2(\Omega)$ broken norm for unstructured discretizations with approximately 400 dofs (non-stabilized Galerkin vs DGM elements).

Pe	ϕ/π	Q_2	$Q-8-2$	Q_3	$Q-12-3$	Q_4	$Q-16-4$
10^2	0	5.66×10^{-2}	9.11×10^{-5}	3.90×10^{-2}	1.35×10^{-5}	2.36×10^{-2}	2.23×10^{-6}
	$\frac{1}{6}$	6.45×10^{-3}	2.30×10^{-4}	3.90×10^{-3}	6.32×10^{-5}	2.05×10^{-3}	1.04×10^{-5}
	$\frac{1}{4}$	6.44×10^{-3}	1.78×10^{-4}	3.79×10^{-3}	2.47×10^{-6}	1.89×10^{-3}	2.42×10^{-8}
10^3	0	4.32×10^{-1}	1.69×10^{-4}	3.64×10^{-1}	2.58×10^{-6}	2.43×10^{-1}	7.84×10^{-7}
	$\frac{1}{6}$	1.49×10^{-2}	3.71×10^{-4}	1.21×10^{-2}	5.51×10^{-5}	9.48×10^{-3}	3.24×10^{-6}
	$\frac{1}{4}$	1.49×10^{-2}	9.62×10^{-5}	1.23×10^{-2}	3.21×10^{-6}	9.83×10^{-3}	3.22×10^{-7}

Table X. Homogeneous boundary layer problem of Section 8.1 with $Pe = 10^6$: relative errors in the $L^2(\Omega)$ broken norm for unstructured discretizations with approximately 400 dofs (non-stabilized Galerkin vs advection-limited DGM elements).

Pe	ϕ/π	Q_2	$\overline{Q-8-2}$	Q_3	$\overline{Q-12-3}$	Q_4	$\overline{Q-16-4}$
10^6	0	7.07×10^{2}	2.23×10^{-2}	6.64×10^{2}	2.23×10^{-2}	5.14×10^{2}	2.22×10^{-2}
	$\frac{1}{6}$	3.20	8.47×10^{-4}	5.15	7.58×10^{-4}	3.45	7.57×10^{-4}
	$\frac{1}{4}$	5.23	7.07×10^{-4}	7.47	7.06×10^{-4}	6.89	7.05×10^{-4}

are two to almost six orders of magnitude smaller than the relative errors associated with the numerical solutions computed with the element Q_4. Also as expected, the higher-order is the DGM element, the lower is the obtained relative error. For the case of the very high Péclet number of 10^6, Table X shows that all of the standard Galerkin elements Q_2, Q_3 and Q_4 fail to deliver acceptable solutions, particularly for $\phi = 0$. On the other hand, the proposed higher-order advection-limited DGM elements deliver solutions with relative errors ranging between 10^{-4} and 10^{-2}.

Finally, Figure 6 compares the nodal values of the solutions computed with the $Q-12-3$ and Q_3 elements when the advection direction is set to $\phi = 0$ and the Péclet number to $Pe = 10^3$.

DOI: 10.1002/nme

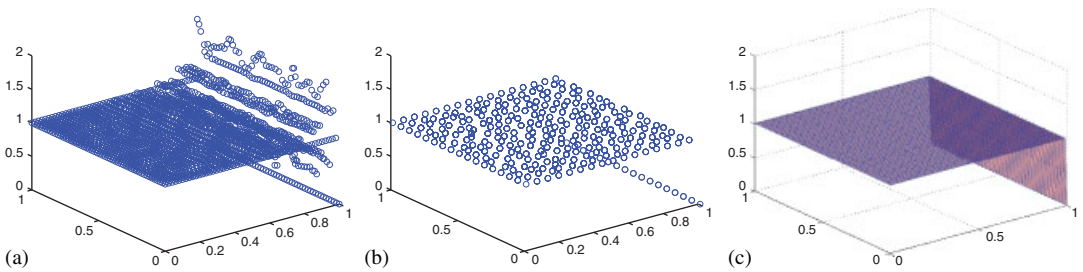

Figure 6. Nodal values of approximated and exact solutions of the homogeneous boundary layer problem of Section 8.1 with $\phi=0$, 1600 dofs and $Pe=10^3$. (a) Q_3; (b) $Q-12-3$; and (c) exact.

Table XI. Homogeneous boundary layer problem of Section 8.2 with $\phi=\pi/7$ and $Pe\leqslant 10^3$: relative errors in the $L^2(\Omega)$ broken norm for unstructured discretizations with approximately 1600 dofs (non-stabilized Galerkin vs DGM elements).

Pe	ψ/π	Q_2	$Q-8-2$	Q_3	$Q-12-3$	Q_4	$Q-16-4$
10^2	0	2.32×10^{-3}	5.79×10^{-5}	9.55×10^{-4}	4.26×10^{-6}	3.79×10^{-4}	4.94×10^{-7}
	$\frac{1}{4}$	1.40×10^{-3}	8.10×10^{-5}	4.93×10^{-4}	9.53×10^{-7}	1.64×10^{-4}	1.30×10^{-8}
	$\frac{1}{2}$	1.18×10^{-3}	4.18×10^{-5}	3.77×10^{-4}	1.01×10^{-5}	1.19×10^{-4}	2.24×10^{-8}
10^3	0	5.92×10^{-3}	1.79×10^{-3}	4.34×10^{-3}	1.10×10^{-4}	3.23×10^{-3}	2.30×10^{-5}
	$\frac{1}{4}$	6.06×10^{-3}	2.54×10^{-4}	4.46×10^{-3}	1.23×10^{-5}	3.29×10^{-3}	8.82×10^{-7}
	$\frac{1}{2}$	5.97×10^{-3}	2.12×10^{-4}	4.36×10^{-3}	1.11×10^{-5}	3.18×10^{-3}	1.59×10^{-6}

The reader can observe that the DGM solution does not exhibit the spurious oscillations that pollute the Galerkin solution.

8.2. Homogeneous boundary layer problem with a flow not aligned with the advection direction

Here, attention is focused on the solution of a homogeneous boundary layer problem with a flow that is *not* aligned with the advection direction. To this effect, the BVP (1) is considered with Dirichlet boundary conditions designed so that the exact solution is

$$u_{ex}(\mathbf{x};\phi,\psi)=\frac{e^{1/2(\mathbf{a}_\phi+\mathbf{a}_\psi)\cdot(\mathbf{x}-\mathbf{1})}-1}{e^{-1/2(\mathbf{a}_\phi+\mathbf{a}_\psi)\cdot\mathbf{1}}-1} \tag{65}$$

where $\phi\in[0,2\pi)$ is the advection-direction and $\psi\in[0,2\pi)$ is an arbitrary flow direction. Again, the domain Ω is taken to be the unit square. It is discretized by unstructured meshes. In all cases, the number of dofs is kept fixed at 1600.

In general, solutions of the form given in (65) are *not* in the span of the enrichment space $\mathcal{V}^E$ described in (23), except for certain values of ϕ and ψ. Here, the advection direction is fixed to $\phi=\pi/7$ and the direction ψ is varied by angles of $\pi/4$ so that the exact solution (65) is not contained in the space of approximation of any of the DGM element considered herein.

Table XI reports for $Pe=10^2$ and $Pe=10^3$ the relative errors associated with the solutions computed on unstructured meshes using the standard Galerkin elements Q_2, Q_3 and Q_4, and the

DOI: 10.1002/nme

Table XII. Homogeneous boundary layer problem of Section 8.2 with $\phi=\pi/7$ and $Pe=10^6$: relative errors in the $L^2(\Omega)$ broken norm for unstructured discretizations with approximately 1600 dofs (non-stabilized Galerkin vs advection-limited DGM elements).

Pe	ψ/π	Q_2	$\overline{Q-8-2}$	Q_3	$\overline{Q-12-3}$	Q_4	$\overline{Q-16-4}$
10^6	0	2.87×10^{-1}	2.07×10^{-3}	1.85×10^{-1}	8.56×10^{-4}	9.84×10^{-2}	6.88×10^{-4}
	$\frac{1}{4}$	2.87×10^{-1}	7.87×10^{-4}	1.85×10^{-1}	5.68×10^{-4}	9.84×10^{-2}	4.61×10^{-4}
	$\frac{1}{2}$	2.87×10^{-1}	9.01×10^{-4}	1.85×10^{-1}	6.77×10^{-4}	9.84×10^{-2}	5.50×10^{-4}

Table XIII. Convergence rates on unstructured meshes (Section 8.2, $\phi=\pi/7$ and $\psi=0$).

Element	Convergence rate ($Pe=10^2$)	Required # dofs to achieve a relative error of 10^{-3} ($Pe=10^3$)
Q_2	2.38	24300
$Q-8-2$	3.27	5400
Q_3	3.48	12500
$Q-12-3$	3.88	850
Q_4	4.41	8600
$Q-16-4$	5.19	570

higher-order DGM elements $Q-8-2$, $Q-12-3$ and $Q-16-4$. In all cases, the DGM elements are reported to outperform their standard Galerkin counterparts (from the computational complexity viewpoint) by a very large margin. The performance results reported in Table XII for $Pe=10^6$ show that the advection-limited DGM elements outperform their standard Galerkin counterparts by even a larger margin of three orders of magnitude in accuracy.

Table XIII reports for the BVP considered herein the convergence rates measured on unstructured meshes for the standard Galerkin and DGM elements at $Pe=10^2$. The DGM elements $Q-8-2$, $Q-12-3$ and $Q-16-4$ deliver roughly cubic, quartic and quintic convergence rates, respectively. Hence from this viewpoint too, these elements are 'comparable' to the standard Galerkin elements Q_2, Q_3 and Q_4, respectively. The performance results reported in Table XIII also show that to achieve a relative error of 0.1% for $Pe=10^3$, the DGM elements $Q-8-2$, $Q-12-3$ and $Q-16-4$ require 4.5, 14.7 and 15.1 times fewer dofs than the standard Galerkin elements Q_2, Q_3 and Q_4, respectively, thereby demonstrating the computational superiority of the DGM methodology.

The aforementioned convergence rates are also graphically depicted in Figure 7. The oscillations in the tail end of the curve for the DGM element $Q-16-4$ is due to the ill-conditioning of this element.

8.3. Two-scale inhomogeneous problem

To highlight the role of the polynomial field u^P in DEM, a non-homogeneous variant of the boundary layer problem defined in Section 8.1 is considered here. More specifically, the source term

$$f(\mathbf{x};\phi)=\mathbf{a}_\phi\cdot\mathbf{1}+|\mathbf{a}|(y\cos\phi+x\sin\phi) \tag{66}$$

DOI: 10.1002/nme

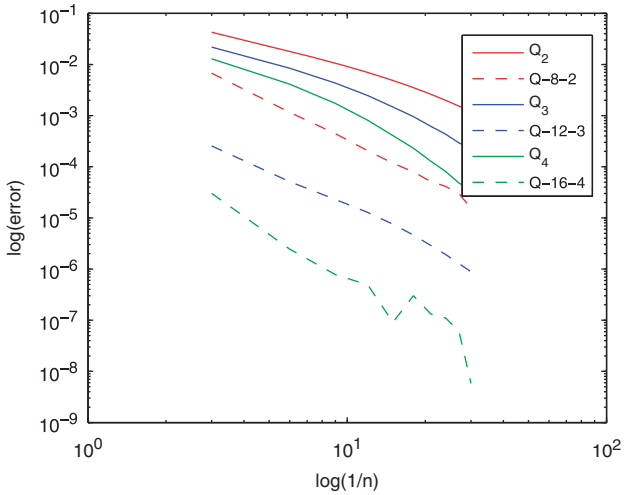

Figure 7. Convergence rates on unstructured meshes (Section 8.2, $\phi=\pi/7$, $\psi=0$ and $Pe=10^2$).

is added and the Dirichlet boundary conditions are designed so that the exact solution to problem (1) is

$$u_{ex}(\mathbf{x};\phi)= \underbrace{\mathbf{x}\cdot\mathbf{1}+xy}_{\text{slowly varying}} + \underbrace{\left(\frac{e^{\mathbf{a}_\phi\cdot(\mathbf{x}-\mathbf{1})}-e^{-\mathbf{a}_\phi\cdot\mathbf{1}}}{e^{-\mathbf{a}_\phi\cdot\mathbf{1}}-1}\right)}_{\text{rapidly varying}} \tag{67}$$

This exact solution contains two scales: a rapidly varying exponential *and* a slowly varying polynomial. Because of this multi-scale behavior, a true DEM element whose approximation basis includes the enrichment as well as the polynomial fields ($u^h=u^P+u^E$) is used to solve this problem.

The performance results obtained for this problem and summarized in Table XIV demonstrate once again the superior accuracy and computational efficiency of the DEM methodology for the solution of inhomogeneous advection–diffusion problems. In particular, Table XV shows that for $Pe=10^6$, the advection-limited DEM elements outperform their standard Galerkin counterparts by an impressive margin.

Table XVI shows that for this two-scale problem, the DEM elements $Q-9-2^+$, $Q-13-3^+$ and $Q-17-4^+$ exhibit convergence rates of approximately 3, 4 and 5, respectively (Figure 8). Therefore, they are comparable from this viewpoint to the standard Galerkin Q_2, Q_3 and Q_4 elements except that they possess dramatically smaller error constants. For $Pe=10^3$, the DEM element $Q-17-4^+$ delivers the same accuracy as $Q-13-3^+$ and $Q-9-2^+$ but using 2.5 and 13.8 times fewer dofs, respectively. This illustrates the higher-order behavior of a DEM element with an increasing value of n^E. Also for $Pe=10^3$, a relative error equal to 0.1% can be achieved by the DEM elements $Q-9-2^+$, $Q-13-3^+$ and $Q-17-4^+$ using approximately 4.75, 14 and 15.1 times fewer dofs than by the Galerkin Q_2, Q_3 and Q_4 elements, respectively. More illustrative than the relative errors reported in Tables XIV and XV are the plots of nodal values of the computed solutions displayed in Figure 9. Whereas even the relatively high-order Q_3 solution

DOI: 10.1002/nme

Table XIV. Inhomogeneous boundary layer problem of Section 8.3 with $Pe \leqslant 10^3$: relative errors in the $L^2(\Omega)$ broken norm for uniform discretizations with approximately 1600 dofs (non-stabilized Galerkin vs DEM elements).

Pe	ϕ/π	Q_2	$Q-9-2^+$	Q_3	$Q-13-3^+$	Q_4	$Q-17-4^+$
10^2	0	1.14×10^{-2}	2.52×10^{-5}	6.02×10^{-3}	1.11×10^{-6}	2.36×10^{-3}	1.09×10^{-7}
	$\frac{1}{4}$	9.23×10^{-4}	1.26×10^{-4}	3.75×10^{-4}	1.51×10^{-5}	1.11×10^{-4}	4.50×10^{-8}
	$\frac{1}{2}$	1.14×10^{-2}	2.40×10^{-5}	6.02×10^{-3}	1.11×10^{-6}	2.36×10^{-3}	4.33×10^{-7}
10^3	0	8.72×10^{-2}	1.39×10^{-4}	6.92×10^{-2}	1.01×10^{-5}	5.22×10^{-2}	3.79×10^{-6}
	$\frac{1}{4}$	4.38×10^{-3}	5.87×10^{-5}	3.36×10^{-3}	1.90×10^{-5}	2.47×10^{-3}	2.00×10^{-6}
	$\frac{1}{2}$	8.72×10^{-2}	1.07×10^{-4}	6.92×10^{-2}	1.01×10^{-5}	5.22×10^{-2}	7.95×10^{-6}

Table XV. Inhomogeneous boundary layer problem of Section 8.3 with $Pe=10^6$: relative errors in the $L^2(\Omega)$ broken norm for uniform discretizations with approximately 1600 dofs (non-stabilized Galerkin vs advection-limited DEM elements).

Pe	ϕ/π	Q_2	$\overline{Q-9-2^+}$	Q_3	$\overline{Q-13-3^+}$	Q_4	$\overline{Q-17-4^+}$
10^6	0	1.20	3.12×10^{-4}	3.81×10^{-1}	8.12×10^{-5}	3.72×10^{-1}	5.12×10^{-4}
	$\frac{1}{4}$	1.52	4.62×10^{-5}	1.49	1.05×10^{-5}	7.05×10^{-1}	1.36×10^{-6}
	$\frac{1}{2}$	1.20	1.87×10^{-5}	3.81×10^{-1}	1.45×10^{-5}	3.72×10^{-1}	1.03×10^{-4}

Table XVI. Convergence rates (Section 8.3, $\phi=\pi/4$).

Element	Convergence rate ($Pe=10^2$)	Required # dofs to achieve a relative error of 10^{-3} ($Pe=10^3$)
Q_2	2.79	14700
$Q-9-2^+$	2.91	3100
Q_3	3.66	8000
$Q-13-3^+$	3.97	570
Q_4	4.65	3400
$Q-17-4^+$	4.95	225

is shown to exhibit spurious oscillations, the DEM $Q-13-3^+$ solution is shown to be virtually indistinguishable from the exact solution in the entire computational domain.

8.4. Double ramp problem on an L–shaped domain

Finally, a variant of the double ramp problem used in [37] for testing stabilized finite elements with mesh refinement is considered here. The domain is an L-shaped region $\Omega=[(0,1)\times(0,1)]\backslash[(0,0.5)\times(0.5,1)]$ (Figure 10). The Péclet number is set to $Pe=10^3$ and the source term of the BVP (1) is set to $f=1$. Homogeneous Dirichlet boundary conditions are prescribed on all six sides of Ω. The advection direction is set to $\phi=0$ and therefore the flow moves from left to

DOI: 10.1002/nme

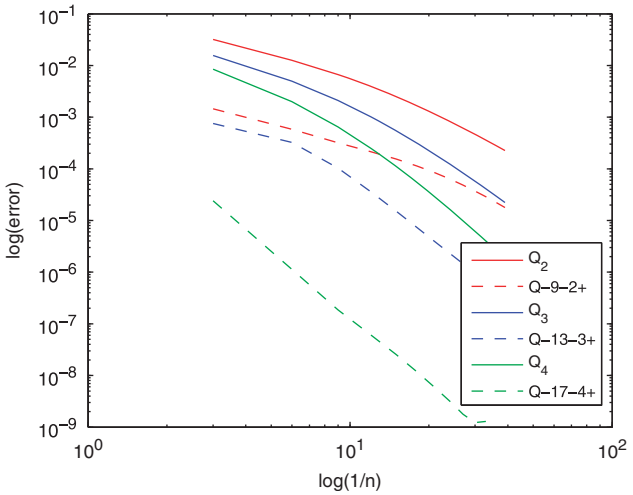

Figure 8. Convergence rates (Section 8.3, $\phi=\pi/4$ and $Pe=10^2$).

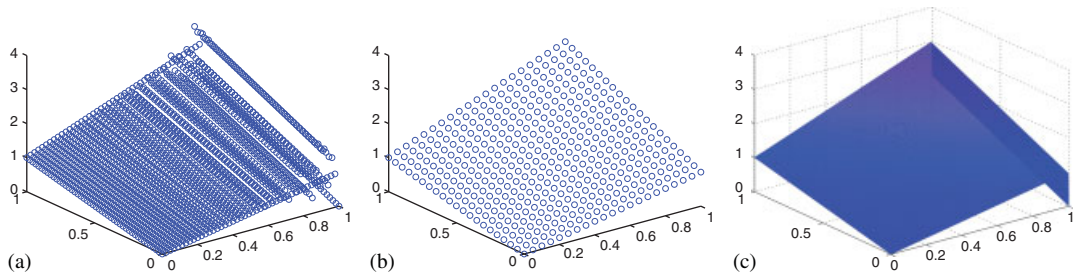

Figure 9. Nodal values of approximated and exact solutions of the non-homogeneous boundary layer problem of Section 8.3 with $\phi=0$, 1600 dofs and $Pe=10^3$. (a) Q_3; (b) $Q-13-3^+$; and (c) exact.

right. The solution of this problem, which is not known analytically, is known however to exhibit a strong outflow boundary layer along the line $x=1$, two crosswind boundary layers along $y=0$ and $y=1$, and a crosswind internal layer along $y=0.5$ (Figure 11). The nature of this solution is therefore different from that of the BVPs considered in the three previous sections. Indeed, this problem is one of the most stringent benchmark problems for advection–diffusion.

A reference solution for this problem that is free from any spurious oscillation is computed on a uniform mesh with 43 200 elements. The performance results of computations on unstructured meshes are reported in Table XVII. They reveal that for this problem, the DGM elements provide only a moderate improvement over the Galerkin elements. However, the DEM elements provide a dramatic improvement of orders of magnitude in both accuracy and computational efficiency.

Figures 12–15 show four cross-sections of the nodal values of the numerical solutions computed using the DGM and DEM elements and their standard Galerkin counterparts. The Galerkin solutions exhibit noticeable oscillations in the $y=$const plane near the outflow boundary. These are even present in the higher-order Q_4 solution. On the other hand, no oscillation is seen in the

DOI: 10.1002/nme

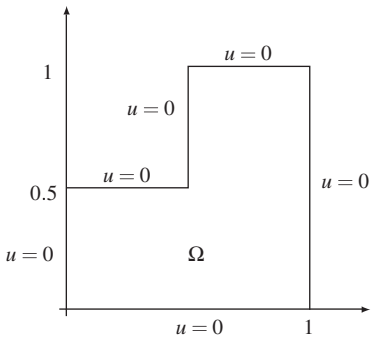

Figure 10. L-shaped domain (Section 8.4).

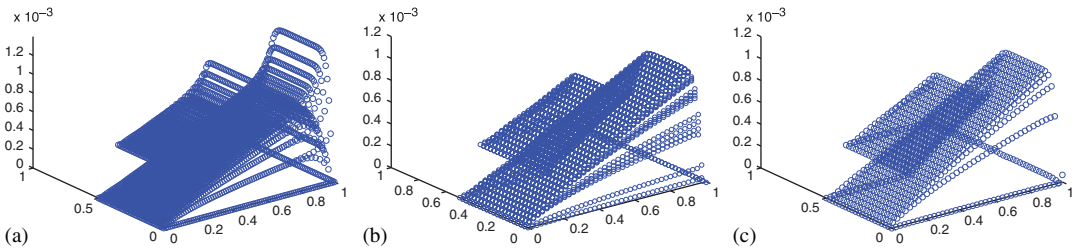

Figure 11. Nodal values of approximated and exact solutions of the homogeneous boundary layer problem of Section 8.4 with $Pe=10^3$ and 1200 elements. (a) Q_3; (b) $Q-12-3$; and (c) $Q-13-3^+$.

computed DGM and DEM solutions. The DGM elements appear to experience a small numerical difficulty but only along the location of the crosswind internal layer (line $y=0.5$) (Figure 13(b)). The polynomial component of the DEM elements appears to resolve this issue completely (Figure 13(c)).

Nodal values of the computed Q_3, $Q-12-3$ and $Q-13-3^+$ solutions are plotted on the entire domain in Figure 11. Again, oscillations are evident in the Galerkin solutions. On the other hand, the DGM and DEM solutions are free from any spurious oscillation.

9. CONCLUSIONS

In this paper, the discontinuous enrichment method (DEM) proposed in [7] for the solution of the two-dimensional advection–diffusion equation is extended to higher-order quadrilateral elements and problems discretized on unstructured meshes. Appropriate Lagrange multiplier approximations on a mesh of quadrilateral elements are designed and the issue of potential redundancy in these approximations in the context of higher-order elements is illuminated and addressed. Three new higher-order pure discontinuous Galerkin method (DGM) quadrilateral elements are constructed and denoted by $Q-8-2$, $Q-12-3$ and $Q-16-4$. The approximation space $\mathscr{V}^h$ of these elements contains only the exponential enrichment field $\mathscr{V}^E$, intended to capture the rapidly varying 'fine' scale that is typically present in the exact solution of advection–diffusion BVPs.

DOI: 10.1002/nme

Table XVII. Double ramp problem of Section 8.4: relative errors in the $L^2(\Omega)$ broken norm ($Pe=10^3$, uniform discretizations, non-stabilized Galerkin vs DGM and DEM elements).

Number of elements	Q_2	$Q-8-2$	$Q-9-2^+$
300	2.72×10^{-1}	1.19×10^{-1}	4.11×10^{-2}
1200	1.23×10^{-1}	6.07×10^{-2}	8.47×10^{-3}
4800	5.26×10^{-2}	2.81×10^{-2}	1.65×10^{-3}
10 800	2.92×10^{-2}	1.54×10^{-2}	7.43×10^{-4}
Number of elements	Q_3	$Q-12-3$	$Q-13-3^+$
300	1.49×10^{-1}	1.11×10^{-1}	2.80×10^{-2}
1200	6.57×10^{-2}	5.00×10^{-2}	4.71×10^{-3}
4800	2.36×10^{-2}	1.02×10^{-2}	8.24×10^{-4}
10 800	1.08×10^{-2}	4.54×10^{-3}	9.75×10^{-5}
Number of elements	Q_4	$Q-16-4$	$Q-17-4^+$
300	9.58×10^{-2}	8.32×10^{-2}	2.16×10^{-2}
1200	3.78×10^{-2}	1.33×10^{-2}	2.94×10^{-3}
4800	1.03×10^{-2}	9.17×10^{-3}	1.26×10^{-4}
10 800	3.70×10^{-3}	4.92×10^{-4}	2.12×10^{-5}

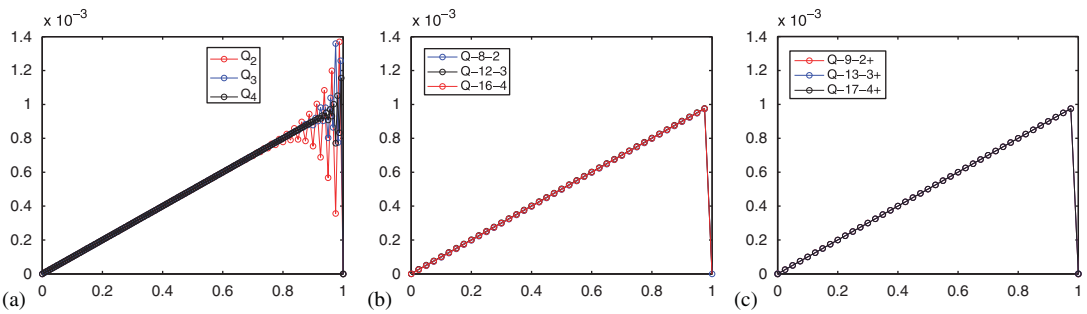

Figure 12. Nodal values of approximated solutions of the L-shaped domain problem of Section 8.4 along the line $y=0.25$ with 1200 elements. (a) Galerkin; (b) DGM; and (c) DEM.

For the finite element solution of inhomogeneous problems, higher-order true DEM elements $Q-9-2^+$, $Q-13-3^+$ and $Q-17-4^+$ are proposed. The approximation spaces of these elements are the direct sum of $\mathscr{V}^E$ and $\mathscr{V}^P$, where $\mathscr{V}^P$ is the polynomial field of the standard Galerkin bilinear quadrilateral element Q_1. Special advection-limited variants of these elements, denoted by $\overline{Q-n^E-n^\lambda}$ and $\overline{Q-n^E-n^{\lambda+}}$, are proposed for the solution of problems in the particularly high Péclet number regime ($Pe>10^3$).

The discontinuous nature of the DGM and DEM approximations enables the static condensation of the enrichment dofs prior to the assembly of the finite element matrices, making the $Q-8-2$, $Q-12-3$ and $Q-16-4$ pure DGM elements (and similarly the $Q-9-2^+$, $Q-13-3^+$ and $Q-17-4^+$ true DEM elements) of comparable computational complexity to the standard Galerkin Q_2, Q_3 and Q_4 elements. It is also found that the aforementioned DGM and DEM elements exhibit

DOI: 10.1002/nme

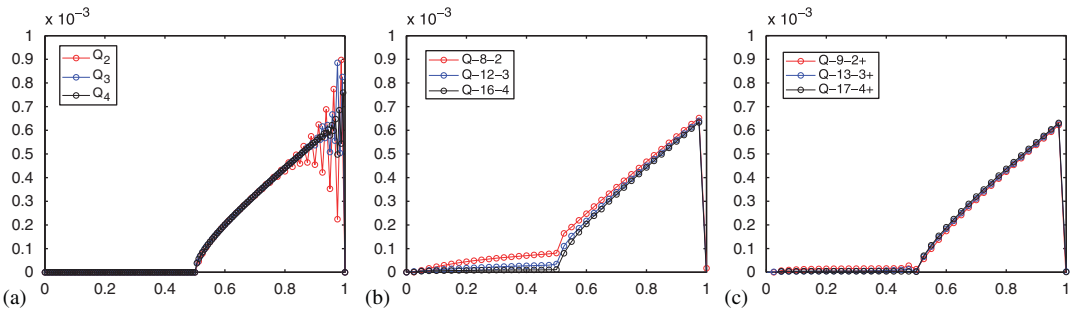

Figure 13. Nodal values of approximated solutions of the L-shaped domain problem of Section 8.4 along the line $y=0.5$ with 1200 elements. (a) Galerkin; (b) DGM; and (c) DEM.

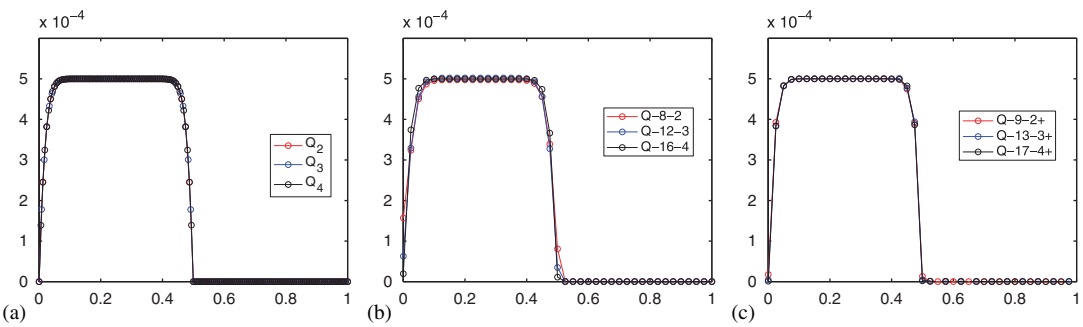

Figure 14. Nodal values of approximated solutions of the L-shaped domain problem of Section 8.4 along the line $x=0.5$ using 1200 elements. (a) Galerkin; (b) DGM; and (c) DEM.

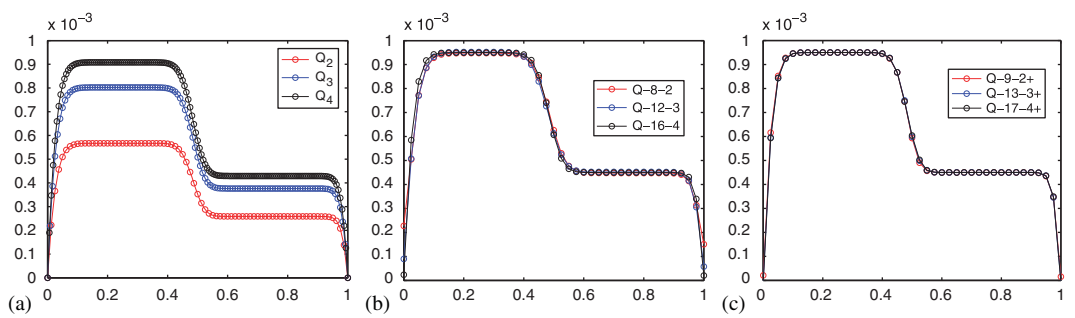

Figure 15. Nodal values of approximated solutions of the L-shaped domain problem of Section 8.4 along the line $x=0.95$ using 1200 elements. (a) Galerkin; (b) DGM; and (c) DEM.

quadratic, quartic and quintic convergence rates, respectively, on both structured and unstructured grids; therefore, they are also comparable to the aforementioned standard Galerkin counterparts from the convergence order viewpoint.

DOI: 10.1002/nme

The proposed DGM and DEM elements are tested on four benchmark problems: a homogeneous boundary layer problem whose exact solution is contained in the approximation space $\mathscr{V}^E$, a homogeneous boundary layer problem whose exact solution is *not* contained in $\mathscr{V}^E$, an inhomogeneous two-scale BVP, and a double ramp problem on an L-shaped domain that exhibits outflow as well as internal boundary layers. For all of these problems, it is found that the DEM elements outperform their standard Galerkin and stabilized Galerkin counterparts of comparable computational complexity by at least one, and sometimes many orders of magnitude in relative error, on both structured and unstructured meshes. For example, it is found that, for $Pe=10^3$, a constant relative error of 0.1% can be achieved using discretizations by the $Q-8-2$ and $Q-9-2^+$ elements using 4 to 5 times less dofs than by the standard Q_2 element. Similarly, it is found that the $Q-12-3$ and $Q-13-3^+$ elements deliver the same accuracy as the Q_3 element but using 14 to 15 times fewer dofs. Most importantly, it is also found that for all considered benchmark problems, the DGM and DEM solutions are almost completely oscillation-free, even in the very high Péclet number regime where the standard higher-order Galerkin solutions are polluted by spurious oscillations. All these results demonstrate the potential of DEM for realistic advection-dominated transport problems in fluid mechanics.

ACKNOWLEDGEMENTS

The first and third authors acknowledge the support by the Office of Naval Research under Grant N00014-08-1-0184. The second author acknowledges partial support by an NDSEG Fellowship sponsored by the U.S. Department of Defense, and partial support by a National Physical Science Consortium (NPSC) Fellowship funded by the Engineering Sciences Center at the Sandia National Laboratories.

REFERENCES

1. Farhat C, Harari I, Franca LP. The discontinuous enrichment method. *Computer Methods in Applied Mechanics and Engineering* 2001; **190**:6455–6479.
2. Farhat C, Tezaur R, Weidemann-Goiran P. Higher-order extensions for a discontinuous Galerkin methods for mid-frequency Helmholtz problems. *International Journal for Numerical Methods in Engineering* 2004; **61**: 1938–1956.
3. Tezaur R, Farhat C. Three-dimensional discontinuous Galerkin elements with plane waves and Lagrange multipliers for the solution of mid-frequency Helmholtz problems. *International Journal for Numerical Methods in Engineering* 2006; **66**:796–815.
4. Zhang L, Tezaur R, Farhat C. The discontinuous enrichment method for elastic wave propagation in the medium-frequency regime. *International Journal for Numerical Methods in Engineering* 2006; **66**:2086–2114.
5. Tezaur R, Zhang L, Farhat C. A discontinuous enrichment method for capturing evanescent waves in multi-scale fluid and fluid/solid problems. *Computer Methods in Applied Mechanics and Engineering* 2008; **197**:1680–1698.
6. Massimi P, Tezaur R, Farhat C. A discontinuous enrichment method for three-dimensional multiscale harmonic wave propagation problems in multi-fluid and fluid-solid media. *International Journal for Numerical Methods in Engineering* 2008; **76**:400–425.
7. Kalashnikova I, Farhat C, Tezaur R. A discontinuous enrichment method for the solution of advection–diffusion problems in high peclet number regimes. *Finite Elements in Analysis and Design* 2009; **45**:238–250.
8. Oliveira SP. Discontinuous enrichment methods for computational fluid dynamics. *Ph.D. Thesis*, University of Colorado, Denver, CO, 2002.
9. Brooks AN, Hughes TJR. Streamline upwind/Petrov–Galerkin formulations for convection dominated flows with particular emphasis on the incompressible Navier–Stokes equations. *Computer Methods in Applied Mechanics and Engineering* 1982; **32**:199–259.
10. Hughes TJR, Brooks AN. A multi-dimensional upwind scheme with no crosswind diffusion. In *Finite Element Methods for Convection Dominated Flows*, Hughes TJR (ed.), vol. 34. Applied Mechanics Division (AMD) American Society of Mechanical Engineers: New York, 1979; 19–35.

DOI: 10.1002/nme

11. Corsini A, Rispoli F, Santoriello A. A quadratic Petrov–Galerkin formulation for advection–diffusion-reaction problems in turbulence modelling. *Journal of Computational and Applied Mechanics* 2004; **5**:237–249.
12. Sheu TWH, Tsai SF, Wang MMT. A monotone finite element method with test space of Legendre polynomials. *Computer Methods in Applied Mechanics and Engineering* 1997; **143**:349–372.
13. Araya R, Behrens E, Rodriguez R. An adaptive stabilized finite element scheme for the advection-reaction-diffusion equation. *Applied Numerical Mathematics* 2005; **54**:491–503.
14. Harari I, Hughes TJR. Galerkin/least squares finite element methods for the reduced wave equation with non-reflecting boundary conditions in unbounded domains. *Computer Methods in Applied Mechanics and Engineering* 1992; **98**:411–454.
15. Hughes TJR, Franca LP, Hulbert GM. A new finite element formulation for computational fluid dynamics: VIII. The Galerkin/least-squares method for advective-diffusive equations. *Computer Methods in Applied Mechanics and Engineering* 1989; **73**(2):173–189.
16. Franca LP, Frey SL, Hughes TJR. Stabilized finite element methods, I. Application to the advective-diffusive model. *Computer Methods in Applied Mechanics and Engineering* 1992; **95**:253–276.
17. Franca LP, Farhat C. Bubble functions prompt unusual stabilized finite element methods. *Computer Methods in Applied Mechanics and Engineering* 1995; **123**:299–308.
18. Babuška I, Melenk JM. The partition of unity method. *International Journal for Numerical Methods in Engineering* 1997; **40**:727–758.
19. Melenk JM, Babuška I. The partition of unity method finite element method: basic theory and applications. *Computer Methods in Applied Mechanics and Engineering* 1996; **139**:289–314.
20. Belytschko T, Black T. Elastic crack growth in finite elements with minimal remeshing. *International Journal for Numerical Methods in Engineering* 1999; **45**(5):601–620.
21. Duarte CA, Reno LG, Simone A. High-order generalized FEM for through-the-thickness branched cracks. *International Journal for Numerical Methods in Engineering* 2007; **72**:325–351.
22. Gracie R, Belytschko T. Concurrently coupled atomistic and XFEM models for dislocations and cracks. *International Journal for Numerical Methods in Engineering* 2009; **78**(3):354–378.
23. Brezzi F, Russo A. Choosing bubbles for advection–diffusion problems. *Mathematical Models and Methods in Applied Sciences* 1994; **4**(4):571–587.
24. Brezzi F, Marini D, Russo A. Applications of the pseudo residual-free bubbles to the stabilization of convection–diffusion problems. *Computer Methods in Applied Mechanics and Engineering* 1998; **166**:51–63.
25. Franca LP, Macedo AP. A two-level finite element method and its application to the Helmholtz equation. *International Journal for Numerical Methods in Engineering* 1998; **43**:23–32.
26. Baumann CE, Oden JT. A discontinuous *hp* finite element method for the Euler and Navier–Stokes equations, Tenth International Conference on Finite Elements in Fluids (Tucson, AZ, 1998). *International Journal for Numerical Methods in Fluids* 1999; **31**:79–95.
27. Babuška I, Baumann CE, Oden JT. A discontinuous *hp* finite element method for diffusion problems: 1-D analysis. *Computers and Mathematics with Applications* 1999; **37**:103–122.
28. Georgoulis EH, Hall E, Houston P. Discontinuous Galerkin methods for advection–diffusion-reaction problems on anisotropically refined meshes. *SIAM Journal on Scientific Computing* 2007; **30**(1):246–271.
29. El Alaoui L, Ern A. Nonconforming finite element methods with subgrid viscosity applied to advection–diffusion-reaction equations. *Numerical Methods for Partial Differential Equations* 2006; **22**(5):1106–1126.
30. Wang S. A novel exponentially fitted triangular finite element method for an advection–diffusion problem with boundary layers. *Journal of Computational Physics* 1997; **134**:253–260.
31. El-Zein A. Exponential finite elements for diffusion–advection problems. *International Journal for Numerical Methods in Engineering* 2005; **62**:2086–2103.
32. Farhat C, Harari I, Hetmaniuk U. A discontinuous Galerkin method with Lagrange multipliers for the solution of Helmholtz problems in the mid-frequency regime. *Computer Methods in Applied Mechanics and Engineering* 2003; **192**:1389–1419.
33. Babuška I. The finite element method with Lagrange multipliers. *Numerical Mathematics* 1973; **20**:179–192.
34. Brezzi F. On the existence, uniqueness and approximation of saddle point problems arising from Lagrange multipliers. *Revie Francaise d'Automatique Informatique Recherche Operationnelle* 1978; **8-R2**:129–151.
35. Brezzi F, Fortin M. *Mixed and Hybrid Finite Element Methods*. Springer: New York, NY, 1991.
36. Harari I, Franca LP, Oliveira SP. Streamline design of stability parameters for advection–diffusion problems. *Journal of Computational Physics* 2001; **171**:115–131.
37. Franca LP, Hwang FN. Refining the submesh strategy in the two-level finite element method: application to the advection–diffusion equation. *International Journal for Numerical Methods in Engineering* 2002; **39**:161–187.

DOI: 10.1002/nme